JGR Space Physics

RESEARCH ARTICLE
10.1029/2021JA029190

Morphology of the Io Plasma Torus From Juno Radio Occultations

A. Moirano[1,2], L. Gomez Casajus[1,3], M. Zannoni[1,3], D. Durante[4], and P. Tortora[1,3]

[1]Department of Industrial Engineering (DIN), Alma Mater Studiorum—Università di Bologna, Forlì, Italy, [2]Now at: Institute for Space Astrophysics and Planetology, National Institute for Astrophysics, Rome, Italy, [3]Interdepartmental Center for Industrial Research in Aerospace (CIRI AERO), Alma Mater Studiorum—Università di Bologna, Forlì, Italy, [4]Department of Mechanical and Aerospace Engineering (DIMA), Sapienza Università di Roma, Rome, Italy

Key Points:

- Density distribution of electrons in the Io plasma torus is derived from the first 15 radio occultations by Juno
- Temporal and longitudinal variabilities in the electron density of the torus are presented
- Density in the Io torus fluctuates over about 50% the average value and the typical time scale of periodic variation is about 430 days

Supporting Information:

Supporting Information may be found in the online version of this article.

Correspondence to:

A. Moirano,
alessandro.moirano@inaf.it

Citation:

Moirano, A., Gomez Casajus, L., Zannoni, M., Durante, D., & Tortora, P. (2021). Morphology of the Io Plasma Torus from Juno radio occultations. *Journal of Geophysical Research: Space Physics*, *126*, e2021JA029190. https://doi.org/10.1029/2021JA029190

Received 28 JAN 2021
Accepted 7 SEP 2021

Abstract The jovian moon Io disperses about 1 ton/s of material in the planetary magnetosphere, mainly by sublimation of SO2 from the surface and by its intense volcanic activity. The ejected material supplies the plasma cloud surrounding Jupiter known as Io Plasma Torus (IPT). The radio communication between Juno and the Earth DSN station crosses the IPT near the closest approach. Being a dispersive medium, the IPT introduces a path delay in the signal, which can be analyzed to retrieve the density distribution of electrons. We used radio tracking data from the first 25 orbits to investigate the morphology of the IPT and its variability. We adopted a static and axisymmetric model for the electron density and we updated it including temporal and longitudinal variability. We found that our best fit model must include both variabilities, even though on average the morphology of the IPT agrees with previous analyses. Our results suggest that the density of the outer region of the IPT fluctuates over 50% the average value over a typical time scale of about 420 days.

1. Introduction

Ten years after the discovery of the magnetosphere of Jupiter, Bigg (1964) pointed out that the modulation in the observed radio emission bursts was related to the phase of Io, the innermost Galilean moon, and so he laid the foundations for the study of the interaction between natural satellites and a planetary magnetosphere.

In the 70s, ground-based spectroscopic observations revealed the presence of neutral sodium associated with Io (Brown & Chaffee, 1974). A few years later, Kupo et al. (1976) detected a toroidal cloud of singly ionized sulphur around Jupiter inside Io's orbit using spectrographic plates, which was thought to be originated in an annular cloud of cold plasma in the same region (R. A. Brown, 1976): this is the first detection of the so-called Io Plasma Torus (IPT). More specifically, only the colder region of the IPT (which we know now to be composed by three main regions) was detected at that time. In the same decade, Hill et al. (1974) theorized the inflation of Jupiter's magnetic field due to centrifugal stress of nearly corotating plasma and formulated the centrifugal equator, which corresponds to the midplane of the cold torus. Because the magnetic equator of Jupiter is tilted with respect to the rotational equator, the tilt of the centrifugal equator is 2/3 the way from the rotational to the magnetic equator.

In 1979 Voyager 1 placed an important milestone by revealing the presence of a new region composed of S2+, S3+, and O2+ from UV spectra (Broadfoot et al., 1979; Sandel et al., 1979), which became known as the warm torus. In addition, Voyager 1 provided the first hard evidence of active volcanism on Io (Smith et al., 1979), which makes the moon the most important plasma source in the magnetosphere of Jupiter. The wealth of data gathered by this mission (Bridge et al., 1979; Scarf et al., 1979; Warwick et al., 1979) pushed Bagenal and Sullivan (1981) to elaborate a model for the distribution of the ion species along the magnetic field lines using a centered tilted dipole and particle measurements. They found that the Io Plasma Torus (IPT) is distributed around the centrifugal equator between about 5 and 9R_J (1R_J = 71,492 km is a Jupiter radius measured at the equator) and that three regions can be distinguished by temperature, electron density and mixing ratios of different ions of oxygen and sulphur. The first region (from Jupiter out) is the cold torus, which has temperature of 2–4 eV, typical density of about 1,000 electrons/cm^3 and typical thickness and radial extension of about 0.1–0.2R_J. Second, there is the ribbon, a narrow region (its radial extension is about or less than 0.1R_J) of bright SII emission with typical density of about 3,000 electrons/cm^3 and

thickness of about $1R_J$. In the outer portion of the IPT there is the warm torus (up to about $9R_J$), whose ions have temperature of about 50 eV, density of about 1000–2000 electrons/cm^3 and it is about $1R_J$ thick. From here afterward, we will express densities as cm^{-3} instead of electrons/cm^3, as we always refer to electron density. Subsequently, Ulysses provided additional data by means of a radio occultation of the IPT in 1992 (M. K. Bird et al., 1992; M. Bird et al., 1993).

A second important milestone was the Galileo mission (1995–2003), which was the first orbiter of the Jupiter system. Its nearly equatorial orbits provided in-situ measurements of plasma, even though the quality of the data was reduced by the failure of its high gain antenna (Bagenal et al., 1997; Gurnett et al., 1996; Hinson et al., 1998). During the epoch of Galileo, Cassini produced high quality spectroscopic data between 2000 and 2001 during its jovian flyby to Saturn. These data were useful to study the temporal and longitudinal variation of the IPT (Steffl, 2004a, 2004b; Steffl et al., 2006, 2008). More recently, Hisaki is surveying the IPT using its extreme ultraviolet spectrometer. These observations led to the detection of temporal changes in the composition and electron density of the torus (Koga et al., 2019; Tsuchiya et al., 2018; Yoshikawa et al., 2017; Yoshioka et al., 2018) and longitudinal asymmetries (Tsuchiya et al., 2019).

Launched in 2011 and arrived at Jupiter in 2016, the Juno spacecraft is the second orbiter of the Jupiter system and the most recent step in the exploration of the Jupiter system. In this paper we will make use of radio occultations performed by the spacecraft since its first orbits and up to February 2020 and acquired during the gravity experiment. Our purpose is using these data to characterize the morphology of the IPT. Juno is performing almost polar orbits around Jupiter in order to explore its unknown polar regions, which are important for mapping the magnetic field of Jupiter up to its surface and for understanding the interaction between the ionosphere of Jupiter, its magnetosphere and the Galilean moons (Bagenal, Adriani, et al., 2017). Furthermore, the orbits of Juno are designed so that each perijove (PJ) is as close as $1.05R_J$ in order to investigate the gravity field of Jupiter and the gravitational tides due to its satellites (Asmar et al., 2017), mainly by Io. The gravity experiment exploits Juno's radio tracking data to determine the orbit of the spacecraft and the gravity field of Jupiter (Durante et al., 2020). Given the orbit geometry, Juno's radio signals traverse the IPT near each PJ. Being a dispersive medium, the plasma—and thus the IPT—introduces a path delay in the radio signal proportional to the total electron content (TEC) along the path of the signal (Bertotti et al., 1993). We used the multifrequency links of Juno to remove the non-dispersive contributions (e.g., Doppler effect, frequency shift due to neutrals) from the path delay in a similar way as done by Phipps and Withers (2017), so the signature in the path delay depends only on the TEC along the line of sight between the spacecraft (sometimes denoted as S/C) and the DSN station (G/S). This method and the unique geometry of the orbits of Juno allow to sample the vertical extension of the IPT at single longitudinal sector for each PJ.

In this paper we will make use of the 15 PJs performed for the gravity experiment during the first 25 orbits in order to update and improve the parameters of an already existing electron density model in which each region (i.e., the cold and the warm torus plus the ribbon) is modeled by a double-Gaussian function (Phipps et al., 2018, 2019, 2020, 2021; Phipps & Withers, 2017). For this purpose, we derived an analytical expression for the TEC which takes into account the slight inclination of the radio signal with respect to the centrifugal equator, exploiting the close proximity of Juno to Jupiter and its nearly polar orbits. This allowed us to retrieve constraints on the radial morphology of the IPT using only radio tracking measurements. In addition, the data coverage allows in principle for a good estimation of the longitudinal modulation of the IPT (Steffl et al., 2006; Tsuchiya et al., 2019) and indications of temporal variability (de Kleer et al., 2019).

2. Method

2.1. Multi-Frequency Radio Occultation

Given a signal emitted with frequency f_0 and recorded later with frequency f, the experienced fractional frequency due to the crossed medium is related to the path delay Δl (Bertotti et al., 1993) and it is due to both dispersive and non-dispersive effects:

$$y = \frac{f - f_0}{f_0} = \frac{1}{c}\frac{d\Delta l}{dt} \tag{1}$$

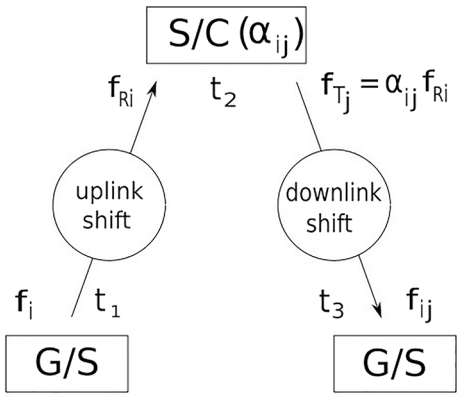

Figure 1. Scheme of a two-way link. The signal is sent in the -band at time t_1 from the G/S and is received by the S/C at time t_2 with a frequency shift $f_i - f_{Ri}$. The signal is sent back upon conversion with the turnaround ratio with frequency $f_{Tj} = \alpha_{ij} f_{Ri}$. In the end, the signal is received by the G/S (which may be different from the starting one) at time t_3 with frequency f_{ij}, which come out of the on-board shift (in order to avoid interference between uplink and downlink) and the shift due to the various media encountered by the signal.

where c is the speed of light. For space communications, this frequency shift is caused by Doppler effect and by the presence of the interplanetary medium (IPM) along the line-of-sight between the spacecraft and the DSN station. The path delay due to the IPM is related to the refractive index n_r of the medium along the raypath $\gamma(\tau)$ by

$$\Delta l = c\int_0^t [n_r(\gamma(\tau),\tau) - 1]d\tau \tag{2}$$

where is the receiving time. For a plasma the index of refraction is a function of the frequency and in the high-frequency approximation, it can be approximated by

$$n_r \approx 1 - \frac{\omega_p^2}{8\pi^2 f_0^2} = 1 - \frac{e^2 n_e}{2\pi m_e f_0^2} \tag{3}$$

where ω_p is the plasma frequency (which depends on the electron density n_e), e is the elementary charge and m_e is the electron mass. Taking into account a frequency of 7.3 GHz (X-band), the high frequency approximation holds if the electron density is below 6.5 x $10^5 cm^{-3}$, which is largely satisfied in both the IPM and the IPT. Substituting the last equation in Equation 2 we find

$$\Delta l = -\frac{ce^2}{2\pi m_e f_0^2}\int_0^t n_e(\gamma(\tau),\tau)d\tau = -\kappa\frac{TEC}{f_0^2} \tag{4}$$

where the total electron content measures the integrated electron density along the line-of-sight direction and thus it has the unit of electrons/cm^2 (or equivalently in TECU = hexems = 10^{16} el/m^2). $\kappa = \frac{ce^2}{2\pi m_e}$ is a constant factor. This last equation can be differentiated with respect to time to obtain the fractional frequency (Equation 1).

A radio occultation experiment takes place whenever a radio signal, traveling from a transmitter to a receiver, passes through a medium, like the IPT. By measuring the properties of the received signal it is possible to study the physical characteristics of the medium. In this paper we exploited the availability of radio links at multiple frequencies between Juno and the Earth. The gravity science instruments include a Ka-band Translator System (KaTS), contributed by the Italian Space Agency, which provides a coherent two-way Ka-up/Ka-down link (34–32 GHz in uplink and downlink respectively). In addition to the Ka/Ka link, the Juno spacecraft telecommunications subsystem supports standard two-way X-up/X-down (7.3–8.4 GHz) link through the Small Deep Space Transponder (SDST). When the KaTS is not used, the SDST can also support a two-way X/Ka (7.3–32 GHz) link, in addition to the standard X/X link. Only two links are available at each occultation, thus we used dual-link techniques to isolate the dispersive contribution due to the plasma (Bertotti et al., 1993; Mariotti & Tortora, 2013).

However, radio tracking of Juno makes use of a coherent link, which means that a signal is sent from the DSN station to the spacecraft, then it is multiplied on-board by a fixed factor (the turnaround ratio) and then it is sent back to the DSN station. A scheme of a two-way link is illustrated in Figure 1. The multiplication is used to avoid interference between the uplink and downlink signal. This method has the advantage that the instrumental precision relies mostly on the station (which can be maintained more easily and in practice has no energy or complexity budget to take into account), thus allowing for a better orbit determination of the spacecraft than a simpler one-way link (which is usually made by means of an ultrastable oscillator). On the other hand, the two-way link is more complicated to use for studying the occulting object, because both legs of the link must be considered (i.e., uplink and downlink), which in principle can introduce different path delay.

In order to find a total fractional frequency which takes into account both uplink and downlink, consider first the two legs separately:

$$y_i^U = \frac{f_{Ri} - f_i}{f_i} \tag{5}$$

$$y_{ij}^{D} = \frac{f_{ij} - f_{Tj}}{f_{Tj}} = \frac{f_{ij} - \alpha_{ij} f_{Ri}}{\alpha_{ij} f_{Ri}} \tag{6}$$

where the apices U and D stands for uplink and downlink, f_i and f_{ij} are the frequencies transmitted (in the i-band) and received (in the j band) by the DSN station, f_{Ri} and f_{Tj} are the frequency received and transmitted by the spacecraft (again, in the i and j band) and α_{ij} is the turnaround ratio. These two equation can be combined together in order to get rid of f_{Ri}, yielding:

$$\alpha_{ij} f_i (y_i^U y_{ij}^D + y_i^U + y_{ij}^D + 1) = f_{ij} \tag{7}$$

We expect the fractional frequency to be smaller than one, so we neglect the term $y_i^U y_{ij}^D$ and we are left with a total fractional frequency

$$Y_{ij} = \frac{f_{ij}}{\alpha_{ij} f_i} - 1 \approx y_i^U + y_{ij}^D \tag{8}$$

Recalling Equation 1, we can distinguish 4 contributions to the total fractional frequency (we use a dot to point out the time derivative):

$$Y_{ij} \approx \frac{1}{c}[(\dot{\Delta l}_{ND}^U + \dot{\Delta l}_{Di}^U) + (\dot{\Delta l}_{ND}^D + \dot{\Delta l}_{Dj}^D)] \tag{9}$$

where ND points out the non-dispersive contributions - due mainly to neutral IPM and Doppler shift—and Di (Dj) the dispersive ones—caused by the plasma—which takes the form of Equation 4. Because of Equation 4, we see that Equation 9 contains information about the TEC: we will apply this equation to different links Juno is able to establish.

2.1.1. X/X-Ka/Ka Link

Radio tracking during most of our PJs are performed in the so-called Dual Uplink-Dual Downlink configuration (Mariotti & Tortora, 2013). As the name suggests, this configuration uses two signals in uplink (for Juno, in X and Ka bands, which approximately correspond to frequencies 7.3 and 34 GHz respectively) and two in downlink (in the same bands as the uplink, but at 8.4 and 32 GHz thanks to the turnaround ratios). Because the non-dispersive contributions in Equation 9 are frequency-independent, we can compute $Y_{XX} - Y_{KaKa}$, so that the non-dispersive contribution cancel out and we are left with a quantity which depends only on the dispersive property of the plasma. Furthermore, we can distinguish the plasma contribution of the IPM and the terrestrial ionosphere from the one of the IPT (assuming other source of plasma to be negligible compared to these). So Equation 9 together with Equation 4 leads to:

$$\begin{aligned} Y_{XX} - Y_{KaKa} = -\frac{\kappa}{c}\Bigg[& \dot{TEC}_{IPM}^U \left(\frac{1}{f_X^2} - \frac{1}{f_{Ka}^2}\right) + \dot{TEC}_{IPM}^D \left(\frac{1}{\alpha_{XX}^2 f_X^2} - \frac{1}{\alpha_{KaKa}^2 f_{Ka}^2}\right) + \\ & + \dot{TEC}_{iono}^U \left(\frac{1}{f_X^2} - \frac{1}{f_{Ka}^2}\right) + \dot{TEC}_{iono}^D \left(\frac{1}{\alpha_{XX}^2 f_X^2} - \frac{1}{\alpha_{KaKa}^2 f_{Ka}^2}\right) + \\ & + \dot{TEC}_{IPT} \left(\frac{1}{f_X^2}\frac{\alpha_{XX}^2 + 1}{\alpha_{XX}^2} - \frac{1}{f_{Ka}^2}\frac{\alpha_{KaKa}^2 + 1}{\alpha_{KaKa}^2}\right)\Bigg] \end{aligned} \tag{10}$$

where we made the assumption that the uplink and downlink contributions of the IPT are the same. Indeed, the time between the uplink and downlink crossing of the IPT by the radio signal is less than 4 s, thus the TEC of the IPT should not change appreciably. On the other side, given that the one-way light time between Earth and Juno is about 40 min, the conditions of the IPM and the ionosphere may have changed between the two legs of the link, therefore their contributions to the TEC could be different.

2.1.2. X/X-X/Ka Link

Two PJs (01 and 13) were performed using a link with a single X-band uplink and downlink in X and Ka bands. We exploit the same method used in Section 2.1.1 in order to get rid of the non-dispersive contribution (i.e., we calculated $Y_{XX} - Y_{XKa}$), but we get rid also of the uplink dispersive contribution. Doing so, the difference between fractional frequency reads

$$Y_{XX} - Y_{XKa} = -\frac{\kappa}{c}(\dot{TEC}^{D}_{IPM+iono} + \dot{TEC}^{D}_{IPT})\frac{1}{\alpha^2_{XX} f^2_{XX}}\left(1 - \frac{\alpha^2_{XX}}{\alpha^2_{XKa}}\right) \tag{11}$$

2.2. Density Models

In order to start our investigation, we adopted the empirical model for the electron density given by Phipps and Withers (2017). In their study, they considered the radial distribution of electrons given by Bagenal and Sullivan (1981) from Voyager 1 and modeled each region with a Gaussian-like distribution centered at the distance of local maximum density (they omit the 1/2 factor at the exponent and we will do the same, but we nevertheless use the shorthand Gaussian for this profile). They noticed that the warm torus cannot be well represented by a single Gaussian model, so they split this region into two pieces: the warm and the extended torus (even though their temperature and chemical composition are the same). Subsequently, they extended their model off the centrifugal equator, modeling the vertical profile of the IPT with another Gaussian for each region in order to take into account the different scale heights.

In this paper we considered the coordinates to be expressed in a left-handed centrifugal frame of reference whose symmetry axis is tilted by 6.8° from the rotation axis at about $\lambda_{III} = 200°$ (System III longitude). We sometimes refer to this frame as "IPT-fixed." Taking cylindrical coordinates in this frame (i.e., z axis aligned with the symmetry axis, r away from Jupiter and λ clockwise), the reference density model reads:

$$\begin{aligned} n(r,z) &= \sum_{i=1}^{3} N_i exp\left[-\frac{(r-R_i)^2}{W_i^2} - \frac{(z-Z_i)^2}{H_i^2}\right] \quad for \quad r \le 6.1R_J \\ n(r,z) &= N_{ext} exp\left[-\frac{(r-R_{ext})^2}{W_{ext}^2} - \frac{(z-Z_{ext})^2}{H_{ext}^2}\right] \quad for \quad r > 6.1R_J \end{aligned} \tag{12}$$

where $i = 1,2,3$ stands for cold torus, ribbon, warm torus and *ext* stands for the extended torus. The parameters of the model are the peak density of each region N, the radial position and extension R and W and the scale height H. The model can be made more realistic by including the parameter Z which takes into account a possible offset of the torus from the centrifugal equator. An estimate of the values of the parameters and density contour plots can be found in Phipps et al. (2018).

However, the above-mentioned model cannot be fully resolved by radio occultations performed by Juno because of the geometry of the observations. Indeed, the shape of the signature in the path delay introduced by the IPT strongly depends on its density gradient in the normal direction from the centrifugal plane and it goes as H_i^{-2}. Taking the values from Table 3 in Phipps et al. (2018), it is easy to see that the density gradient of the cold torus is about two order of magnitude larger than the one of the ribbon, the warm and the extended torus. These latter three regions on the contrary have similar thickness, thus their signatures are quite mixed up by the occultation geometry. This issue was also pointed out by Phipps et al. (2018), hence we make use of a simplified model with a single region to represent the ribbon, the warm and the extended torus, as done for the analyses of PJ 01, 03, 06, 08 10, 11, 14, and 15 (Phipps et al., 2018, 2019, 2021). We will call this region the outer torus and the whole model is given by

$$\begin{aligned} n(r,z) &= N_1 exp\left[-\frac{(r-R_1)^2}{W_1^2} - \frac{(z-Z_1)^2}{H_1^2}\right] \quad r \le 5.5R_J \\ n(r,z) &= N_2 exp\left[-\frac{(r-R_2)^2}{W_2^2} - \frac{(z-Z_2)^2}{H_2^2}\right] \quad r > 5.5R_J \end{aligned} \tag{13}$$

In the Supporting Information S1, we showed that this density profile and the model presented in (Phipps et al., 2018, Appendix A) are both well suited to describe the data within the uncertainty. In turn this also confirms that we are not able to resolve the outer part of the torus in its subregions.

Both Equations 12 and 13 are axially symmetric and static in a centrifugal frame, but in general the torus parameters may be functions of time and longitude in an IPT-fixed frame. This implies that the parameters of those equations can be considered as the "zeroth-order" and that they can be expanded using a Fourier series of time and longitude. One of our main goals is to improve the axisymmetric model including both

longitudinal and temporal periodicities. If we consider a parameter in Equations 12 or 13 which is function of both longitude λ in the centrifugal-fixed frame and time t, its Fourier expansion of order $M_{max} + N_{max}$ reads

$$\sum_{m=0}^{M_{max}} \sum_{n=0}^{N_{max}} A_{m,n} cos(m\lambda) cos\left(\frac{2\pi nt}{T}\right) + B_{m,n} sin(m\lambda) cos\left(\frac{2\pi nt}{T}\right) + \\ + C_{m,n} cos(m\lambda) sin\left(\frac{2\pi nt}{T}\right) + D_{m,n} sin(m\lambda) sin\left(\frac{2\pi nt}{T}\right) \tag{14}$$

where $A_{m,n}$, $B_{m,n}$, $C_{m,n}$ and $D_{m,n}$ are the coefficients of the expansion.

The value of T, the period, is not straightforward, as the IPT exhibits temporal variability on different time scales (M. E. Brown, 1995; Thomas, 1993), ranging from a few hours to a few years. On one side, we are not able to resolve the shortest variabilities because Juno is performing occultations every 53 days in the best case (we used data only when a dual link is available). On the other hand, we cannot use a period T longer than half the data coverage (about three years and half). It is worth pointing out that many observations on the variability of the IPT made use of emission spectra, which strongly depends on the ionic composition, density and temperature. In order to explain these spectroscopic variations, Steffl et al. (2008) and Hess et al. (2011) assumed two hot electron population rotating at different rates: one fixed with Jupiter System III and the other, slower, rotating with a period between System III and System IV. The hot electron population fraction in these paper is of order 0.2%, which is enough to explain azimuthal and temporal variability of line intensity and composition ratios of various species, but it cannot greatly affects the observed TEC directly. Nevertheless, the hot electrons affects the ionization states of the main elements of the IPT such as sulphur and oxygen, therefore it can also influence the electron content (Steffl et al., 2006). More recently, de Kleer et al. (2019) attempted to correlate the volcanic activity of Loki Patera detected in the infrared-band with periodic changes of Io's eccentricity ($T \approx 480$ days) or semimajor axis ($T \approx 460$ days) using three decades of observations. They found that the best fit period for the observed volcanic activity was about 454 days. Because these timespans can be investigated using our data set, we used this last as initial values for T. Indeed, plasma in the IPT is mainly supplied by outgassing from Io and sublimation of SO_2 from the surface (Tsuchiya et al., 2018), whose neutrals are ionized by collisions with already-existing plasma and photoionization, thus an enhanced volcanic activity may affect the IPT changing its density, temperature and composition (Delamere et al., 2004; Hikida et al., 2020; Koga et al., 2019). Nevertheless, the correlation between Io's volcanism and IPT is very thorny. First of all, the brightness of a volcanic events is not necessarily proportional to its emission of gas and dust. Second, Io hosts different types of volcanic activity such as caldera-like formations, flow-dominated eruptions, explosive events and plumes (Davies, 2001; Lopes & Williams, 2015). Each of them is more or less regular and exhibits different magma, gas and dust supply. Third, the altitude, longitude and latitude of an ejection affect the interaction between the outgassing and the torus, determining if new material is ionized or if it fall back on Io's surface (McDoniel et al., 2019). As a last warning, the response of the IPT to plasma injection of different composition, temperature and density may be complex and it is still debated and under observation (Tsuchiya et al., 2018; Yoshikawa et al., 2017; Yoshioka et al., 2018). Thus any agreement with the periodicity of Loki Patera or typical orbital periods of Io should be taken as a mere indication. With these cautions, we tested a model with T as a free parameter to be determined.

In this study, we used a static axisymmetric profile of the density as reference model and we tested the model obtained by setting $M_{max} = 1$ and $N_{max} = 1$ in Equation 14. This is the lowest order of the Fourier expansion that includes both temporal and longitudinal variations and we will refer to this model as *mixed model*.

2.3. Analytical TEC Model

In Phipps and Withers (2017), the occultation geometry undergoes two simplifications in order to calculate the TEC. First, the line of sight between Juno and the DSN station was assumed to be parallel to the centrifugal equator, which is reasonable because of the relatively small angle of the centrifugal equator with respect to the ecliptic plane. Nevertheless, the TEC obtained by integration along such lines of sight is insensitive to the radial parameters R and W. Second, they considered the projection of the trajectory of Juno on a meridional plane in order to integrate the density (see, for example, Figure 1 of Phipps et al., 2018). Actu-

ally, the path of the radio signal is azimuthally slanted with respect to the surface of the IPT, thus it crosses different longitudes at each instant. Therefore in principle we must take into account the full 3D geometry of the occultations (Phipps et al., 2018, 2019, 2021). Nonetheless, we show that it is possible to reduce the problem in two dimension exploiting the close proximity of Juno to Jupiter introducing only a small error. Detailed calculation on how such reduction was performed can be found in the Supporting Information S1.

First, we performed the projection of the S/C position on a proper meridional plane. The plane we are considering is perpendicular to the centrifugal plane and passes through the G/S position at each instant and the center of mass of Jupiter (see Figure S1). We then evaluated the projection of the S/C position onto this plane and we made use of this approximate trajectory of Juno to carry out the integration. We evaluated the error introduced by such approximation by using the IPT described by Equation 12 and simulating the occultations performed by Juno. For each occultations we found that the relative difference between the TEC computed with the full 3D geometry and the one obtained with the approximation is usually less than 1% and almost never greater than 5%, except far from the occultation, where $TEC \to 0$, thus making the relative error large even though the absolute TEC difference is small. Given that the uncertainty we estimated for our data set is always greater than 5% of the minimum path delay, this has negligible consequence on the parameter estimation.

Second, we integrated the density profile in Equation 13 using the parametrization $r \to \rho, z \to m\rho + q$, where ρ is the radial coordinate in the meridional plane away from Jupiter, m is the angular coefficient of the line of sight between S/C and G/S and q is the intercept with the z-axis of the IPT-fixed frame. In the end, we were able to obtain an analytic expression for the TEC:

$$\begin{aligned} TEC &= \int_{\gamma} n(r,z)dl = \int_{R_{sc}}^{R_{gs}} n(\rho, m\rho+q)\sqrt{1+m^2}\,d\rho = \\ &= N_1 W_1 H_1 \sqrt{\frac{\pi(1+m^2)}{4(m^2W_1^2+H_1^2)}} exp\left[-\frac{(mR_1 - Z_1 + q)^2}{m^2W_1^2+H_1^2}\right] \times \\ &\times \left[erf\left(\frac{H_1^2(R_1-\rho) + W_1^2(m^2\rho - Z_1 m + qm)}{H_1 W_1 \sqrt{m^2W_1^2+H_1^2}}\right)\right]_{R_{sc}}^{5.5R_J} + \\ &+ N_2 W_2 H_2 \sqrt{\frac{\pi(1+m^2)}{4(m^2W_2^2+H_2^2)}} exp\left[-\frac{(mR_2 - Z_2 + q)^2}{m^2W_2^2+H_2^2}\right] \times \\ &\times \left[erf\left(\frac{H_2^2(R_2-\rho) + W_2^2(m^2\rho - Z_2 m + qm)}{H_2 W_2 \sqrt{m^2W_2^2+H_2^2}}\right)\right]_{5.5R_J}^{R_{gs}} \end{aligned} \tag{15}$$

where $[f(\rho)]_a^b = f(b) - f(a)$ and R_{sc} and R_{gs} are the radial position of the S/C and the G/S respectively. Here γ is the line of sight between the projected S/C position and the G/S. This way we can plug Equation 15 into Equation 4 and obtain a relation between the observed path delay and the TEC along the line of sight between Juno and the DSN station.

2.4. Parameter Estimation

Two different technique were used to estimate the typical parameters of the IPT in Equation 13: the single arc fit and the global fit. In the first case, each path delay signature is fitted individually with the delay obtained from Equations 4 and 15, where m and ρ are computed from the position of the S/C and the DSN station as function of time. Using the single arc technique each PJ is characterized by its own set of parameters, which is different from one another. Example of this approach can be seen in Phipps et al. (2019, 2021). The main advantages of this method are its simplicity (there are few parameters to be estimated) and that the resulting residuals are within the uncertainty of the data (see Figures 10–12 in Phipps et al., 2019 and Figure 5 in this paper). The single arc approach has also some limitations: in the case under study, the model cannot include temporal and longitudinal variability on typical scales longer than the one spanned by a single occultation (i.e., $\tau > 2hr$ and $\Delta\lambda_{III} > 70°$). Besides, the parameters R and Z in Equations 13 and 15 are geometrically coupled as can be seen schematically in Figure 2. The global fit approach instead tries to fit all the data using a single set of parameters to characterize the IPT. This technique makes the parameters R and

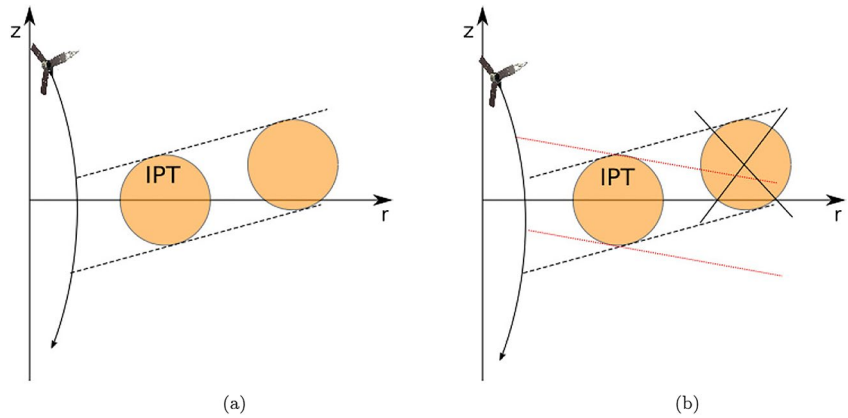

Figure 2. Sketch of the ambiguity on the Io Plasma Torus (IPT) position using a single arc approach (left panel) and how an additional occultation tilted with a different angle with respect to the centrifugal equator can decouple the offset Z from the radial position R (right panel). The curved line is the schematic trajectory of Juno moving southward, the black dotted lines are the radio signal toward the DSN station right before and after an occultation. The red dotted lines have the same meaning as the black ones, but for a different occultation. The orange disc represents the position of the IPT. The black cross in the right panel represents the wrong position of the IPT.

Z in Equations 13 and 15 to be decoupled if the line of sight between Juno and the DSN station has different tilt from one PJ to the other. Furthermore, it allowed us to exploit all the timespan and the sector coverage (see Section 2.5) to include temporal and longitudinal variability in the model. Indeed, the model used for a global fit must include all the effects that govern the variability of the IPT, many of which are still unknown. In turns, including all such effects lead to very complex models which may make the fitting algorithm to not converge due to the nonlinear nature of the model. In this study, we show results from both approaches. Since R and Z are coupled, we first need an estimate of R_1 and R_2 for the single arc fit using Equation 15. We take these values from Voyager 1 data Bagenal and Sullivan (1981), thus we fixed $R_1 = 5.2R_J$ and $R_2 = 5.7$ R_J. This last was chosen by fitting the radial profile of the electron density reported by Voyager (Bagenal & Sullivan, 1981) from $5.5R_J$ outward with a single gaussian. Additional details regarding the fit to the radial profile of the electron density can be found in the Supporting Information S1.

Looking at Equation 15, we notice that the parameter W is coupled to N in the linear coefficient and it appears in the gaussian parameter $\sigma^2 = m^2W^2 + H^2$, where m is the angular coefficient of the line of sight between Juno and the G/S. Given that $m^2 < 0.033$ over all the PJs, the width of the signature is very little sensitive on W and it can be modeled approximately by $\sigma \approx H$. This in turn makes N to be undetermined. The error function in Equation 15 is of little use because it is nearly constant over the time window of the occultations. Thus we decided to fix the value of $W_1 = 0.2R_J$ and $W_2 = 1.5R_J$ in Equation 13. These values are obtained from Voyager 1 data (Bagenal & Sullivan, 1981) and the above-mentioned gaussian fit we used to estimate R_2 for the single arc fits.

During each occultation the radio signal crosses three main plasma sources which affect the path delay: the Earth's ionosphere, the IPM and the IPT. Thus, in order to fit the signature of the IPT, we first need to remove the contribution due to the other two sources. In addition, the DSS-25 of the DSN showed a differential delay between the X and Ka-band during uplink, which strongly affect the path delay estimated by radio tracking data in a dual uplink dual downlink configuration (see Figure 7 of Zannoni, 2020). In this study, we will use an estimate of this delay performed at JPL in November 2018 (Buccino et al., 2019).

The ionospheric delay is removed by means of GPS data (Thornton & Border, 2000), thus our main concern is removing the plasma contribution due to the IPM, whose main source is the solar wind. Its high variability (Ebert et al., 2014; Matthaeus et al., 1991) makes difficult to determine its impact on the delay. If we consider the density of the solar wind to be a decreasing function only of the radius from the Sun (e.g.,: Köhnlein, 1996), the time derivative of the TEC depends only on the relative motion of the S/C and the G/S. For the time interval of a single PJ (about 6–8 hr), this means that we could, in principle, fit the solar wind contribution with a straight line whose slope depends on the relative velocity of S/C and G/S.

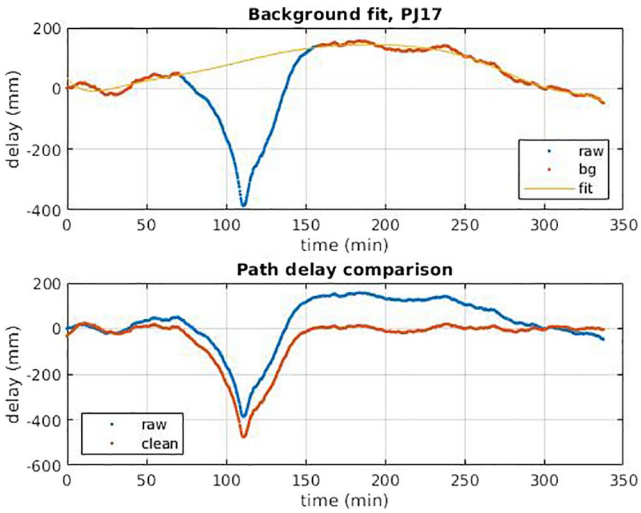

Figure 3. Example of the background contribution removal from the path delay during PJ17 using a 9th degree polynomial. In the top panel the dotted curve is the raw path delay: the red dots are the background used for the fit (yellow line). In the bottom curve the raw path delay (blue dots) is compared with the background-free path delay (red line).

Actually, the path delay far from the signature of the IPT shows other signatures which cannot be ascribed to a linear drift due to G/S-S/C relative motion in a stationary solar wind. The fluctuations observed in the path delay may be due to specific conditions of the electron content along the line of sight between Juno and the DSN station that are not measurable. We empirically removed this effect by fitting a nine-degree polynomial as already done in previous data analysis of Juno radio occultations (Phipps et al., 2019, 2021). We substituted the signature of the IPT with a linear interpolation between the beginning and the end of it and we used this path delay to remove the background. The linear interpolation stabilizes the fit, while leaving missing data can make the fit to exhibit strong fluctuations. In Figure 3, an example of the background removal during PJ17 can be inspected. In this way we calibrated for the solar wind contribution taking into account an unknown variability, maybe due to different periods of solar activity, longitudinal asymmetries in the solar wind or time-specific events.

Once we get rid of the background contributions to the path delay, we use a Markov Chain Monte Carlo algorithm coded in MATLAB to fit the data (Haario et al., 2001, 2006). This code combines the delayed rejection algorithm (DR, which derives from the Metropolis-Hastings algorithm) with the adaptive metropolis algorithm (AM) and it is thus referred as DRAM (Haario et al., 2006).

For the single arc fits we started from a uniform distribution for each parameter. We chose $N_1 = 1500\ cm^{-3}$ and $N_2 = 2500\ cm^{-3}$ as initial values, with upper and lower boundary [0, 3,000]cm^{-3} for N_1 and [1000, 7,500] cm^{-3} for N_2. These values were taken in agreement with typical density of the IPT of a few thousands electrons for cm^{-3} (Bagenal et al., 1997; Bagenal & Sullivan, 1981; M. Bird et al., 1993). For the scale height H_i, the initial values $H_1 = 0.2\mathrm{R}_J$ and $H_2 = 1.0\mathrm{R}_J$ were taken approximately from Phipps et al. (2019, 2021), while their respective boundaries were set at [0.05 0.4]R$_J$ and [0.5, 1.3]R$_J$ respectively. For the offsets, we started from $Z_1 = Z_2 = 0R_J$ with upper and lower boundary at $[-0.3, 0.3]\mathrm{R}_J$.

We used uniform distributions also for the global fits. For the axisymmetric model the initial values of $N_1 = N_2 = 3000cm^{-3}$ were chosen in agreement with the single arc fits and they were bounded between 500cm^{-3} and 5,000cm^{-3}. The initial value of $H_1 = 0.2R_J$ and $H_2 = 1.0R_J$ were the same as in the single arc approach with upper and lower boundary of [0.05, 0.5]R$_J$ and [0.5, 1.5]R$_J$ respectively. For the radial position we choose $R_1 = 5.2R_J$ and $R_2 = 5.7R_J$ in agreement with the parameter fixed in the single arc fits; their boundary were [4.5, 5.9]R$_J$ and [5.2, 7.0]R$_J$ respectively. For the offsets we assumed as a starting point $Z_1 = Z_2 = 0R_J$ and they can both span the interval $[-0.3, 0.3]\mathrm{R}_J$.

For both the single arc fits and the global fit of the axisymmetric model we adopted boundaries as large as possible for the algorithm to converge within $2 \cdot 10^5$ iterations.

After we retrieved the parameters from the fit of the axisymmetric model, we used them as input for the mixed model. We reduced the parameter space to help the convergence of the algorithm: for the cold torus parameters we choose the boundary to be at about three times the uncertainty from the axisymmetric model, while for the outer torus we set the boundary at five times the uncertainty. Indeed, we expanded only N_2 and H_2 using Equation 14 as the outer torus is the main responsible of the depth and width of the signature and to keep the model as simple as possible, thus we left a larger space for the parameters of this region to allow them to change more freely. The first and second order coefficients in Equation 14 are normalized to the zero order coefficient and their boundary are set at −0.5 and 0.5. The period T in Equation 14 is left as a free parameter with initial value $T = 450$ days, which is taken approximately from the result of de Kleer et al. (2019). The boundary are based on the time spanned by our data set: the lower limit is given by twice the maximum time between two subsequent PJs (about 300 days) and half of the time between PJ01 and PJ25 (about 630 days). Summaries of initial values and boundaries used for the global fits can be found in Table 2.

Table 1
Epoch and Longitude of Each Perijov

PJ	*Date*[a]	*Start*[b]	*CA*[b]	*End*[b]	*LongCA*[c]	*Long Peak*[c,d]
01	2016-08-27	10:52	13:43	18:52	188°	195°
03	2016-12-11	12:34	17.52	19:18	77°	66°
06	2017-05-19	01:25	06:38	09:45	215°	222°
08	2017-09-01	19:34	22.39	03:09	27°	18°
10	2017-12-16	14:24	18.46	21:08	341°	335°
11	2018-02-07	11:21	14:33	18:03	242°	248°
13	2018-05-24	03:48	06:18	10:54	70°	51°
14	2018-07-16	00:10	05:59	07:15	117°	116°
15	2018-09-06	21:18	02:00	03:58	22°	13°
17	2018-12-21	16:16	17:50	21:54	179°	189°
18	2019-02-12	13:27	18:18	19:09	247°	254°
21	2019-07-21	02:22	04:37	08:29	296°	298°
22	2019-09-11	23:09	04:24	05:04	342°	333°
23	2019-11-03	20:31	23:04	02:04	196°	209°
25	2020-02-17	15:10	18:39	20:54	130°	140°

[a]The dates (yyyy-mm-dd) refer to the day when the tracking started. [b]The times are referred to UTC DSN station time (t_3 in Figure 1). [c]The longitude is referred to System III. [d]Each occultation is $\pm(30° - 40°)$ from the peak density.

To evaluate the weight to use for our measurements, we consider three different contributions: solar wind scintillation, ionosphere and background fluctuations. The uncertainty due to scintillation of the solar wind is given by numerical integration of the uncertainty in the Doppler shift in the *X*-band and it is a function of the SEP angle (Sun-Earth-Probe) (Iess et al., 2014). The error on the TEC due to the terrestrial ionosphere depends on the elevation of the spacecraft and it ranges from 3 TECU at high elevation to 8 TECU below 10°. Since we did not included the elevation in computing the line of sight between Juno and DSN station, in this study we adopted the average uncertainty $\Delta TEC_{iono} = 5\text{TECU}$ (Thornton & Border, 2000). The background fluctuations are more evident in some PJs than others. These may be caused by anomalous conditions in the solar wind which may be time-specific and localized. In order to take into account these fluctuations we use the RMS of the residuals obtained from a linear fit to the background plasma. We did not use the 9th degree polynomial used for the background removal because it absorbs also the fluctuations, thus the residuals are very similar among the occultations and so the resulting weights.

2.5. Data

Our investigation of the IPT uses PJs dedicated to the gravity experiment. Indeed the closest the flyby is to Jupiter, the more relevant the gravity field becomes on the trajectory of the spacecraft. Besides, given the morphology of the IPT, the gravity experiment and the occultations of the IPT occur in the same time windows. So far, we have made use of 15 PJs (Table 1), which allowed us to span more than 3 years since August 2016 (PJ01) to February 2020 (PJ25). Plots of the signature of the IPT in the path delay data can be seen in Figure 5. The gray area represents the uncertainty estimated as explained in the end of Section 2.4. As can be noticed, the minimum value of the delay after the background removal varies between −300 and −600 mm, which points out strong variations in the TEC of the IPT over the three years of observations. Because Juno is performing occultations every ~53 days and that each occultation spans a limited longitudinal sector, such variability can be due to longitudinal asymmetry and/or temporal periodicities.

The path delay of PJ01 and 13 in Figure 5 appears shallower compared to the other since they were measured using a X/X-X/Ka link, so they are due only to the plasma crossed in downlink. If the tracking during these PJs had been performed using a X/X-Ka/Ka link, their signature would have been about 2.25 as deep.

Table 2
Table of the Results Obtained With the Global Fits

	Mixed			Axisymmetric		
params	*init.*(*mix*)	*LB*/*UB*(*mix*)	*best*(*mix*)[a]	*init.*(*ax*)	*LB*/*UB*(*ax*)	*best*(*ax*)[a]
N_1 (cm^{-3})	1783	1,000/2,500	1993 ± 185	1800	100/2,700	$1,783 \pm 239$
R_1 (R_J)	5.20	5.0/5.4	5.19 ± 0.06	5.2	4.8/5.4	5.20 ± 0.06
H_1 (R_J)	0.20	0.1/0.3	0.21 ± 0.02	0.2	0.1/0.4	0.20 ± 0.03
N_2	2554	2,000/3,000	2429 ± 68	2,200	1,500/4,000	$2,554 \pm 105$
R_2	5.73	5.5/6.0	5.68 ± 0.04	5.7	5.5/6.0	5.73 ± 0.05
H_2	0.90	0.8/1.0	0.89 ± 0.02	0.9	0.8/1.3	0.90 ± 0.03
A_{10}^{N2}	0.0	−0.5/0.5	-0.28 ± 0.04			
B_{10}^{N2}	0.0	−0.5/0.5	0.31 ± 0.03			
A_{01}^{N2}	0.0	−0.5/0.5	0.07 ± 0.04			
C_{01}^{N2}	0.0	−0.5/0.5	-0.10 ± 0.04			
A_{11}^{N2}	0.0	−0.5/0.5	0.25 ± 0.06			
B_{11}^{N2}	0.0	−0.5/0.5	0.34 ± 0.04			
C_{11}^{N2}	0.0	−0.5/0.5	-0.2 ± 0.1			
D_{11}^{N2}	0.0	−0.5/0.5	0.0 ± 0.1			
A_{10}^{H2}	0.0	−0.5/0.5	0.10 ± 0.03			
B_{10}^{H2}	0.0	−0.5/0.5	0.03 ± 0.03			
A_{01}^{H2}	0.0	−0.5/0.5	-0.10 ± 0.05			
C_{01}^{H2}	0.0	−0.5/0.5	0.12 ± 0.06			
A_{11}^{H2}	0.0	−0.5/0.5	-0.09 ± 0.09			
B_{11}^{H2}	0.0	−0.5/0.5	0.03 ± 0.06			
C_{11}^{H2}	0.0	−0.5/0.5	0.22 ± 0.08			
D_{11}^{H2}	0.0	−0.5/0.5	-0.08 ± 0.05			
T (days)	450	317/635	432 ± 2			

Note. The columns 2–4 refer to the mixed model and they represent the initial value (*init.*), the upper and lower boundaries (*UB* and *LB*), the best fit value from the MCMC algorithm with the 1-σ uncertainty (*best*) respectively. The columns 5–7 are the same, but for the axisymmetric model.
[a]The uncertainties were adapted after the stability test.

This scaling comes from the factor $(\alpha_{XX}^2 + 1) - (\frac{\alpha_{XX}^2 f_X^2}{\alpha_{KaKa}^2 f_{Ka}^2})(\alpha_{KaKa}^2 + 1)$ in Equation 10. This factor of has been included in the fitting algorithm, so that we fitted all the data as they were acquired using only the X/X-Ka/Ka link. Nevertheless, in Section 3 we report the actual path delay extracted using the multifrequency technique (Bertotti et al., 1993; Mariotti & Tortora, 2013), therefore the signatures of PJ01 and 13 show only the downlink plasma contribution.

Even though the polar orbits of Juno change gradually in longitude, so far the radio signals have spanned many sectors of the IPT, as can be seen in Figure 4.

3. Results

In this section, we present the result obtained using the single arc approach and the global fit described in Section 2.4. Establishing the convergence of a Monte Carlo chain is still an open problem, as there is no unique way to determine if the chain has converged to the target distribution. Only a handful of diagnostic

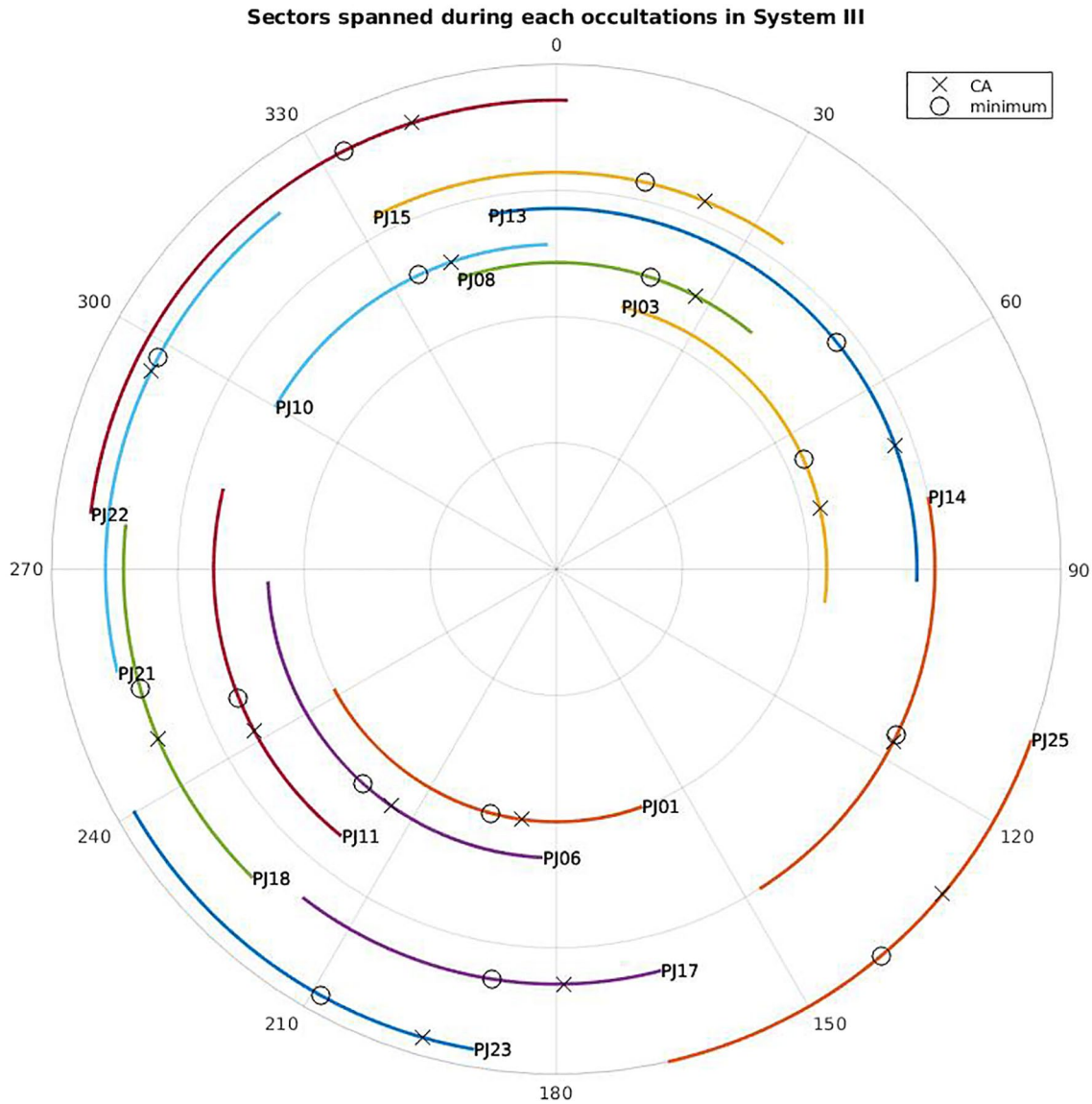

Figure 4. System III longitudinal sectors spanned by *Juno* during each labeled occultation. The radial direction points toward increasing time (not in scale). Black crosses point out the longitude of closest approach, while black circles the minimum of the path delay.

tool are available (e.g., Cowles & Carlin, 1996). In this study, we considered a small autocorrelation of the chain as diagnostic for the convergence.

The equilibrium parameter distributions we obtained are all univariate and they are gaussian-shaped in nearly all the cases.

In order to quantify the difference between the axisymmetric and other models, we reported the difference between the square root of the mean weighted sum of squared residuals (MWSSR) of the axisymmetric model and the MWSSR of the mixed model. These values can be found alongside the plots in Figure 7. The MWSSR is computed as

$$MWSSR = \sqrt{\frac{\sum_i^L W_i (O_i - E_i)^2}{L - N}} \tag{16}$$

where W_i, O_i and E_i are the weight, the observed value and the expected value (from the fit) of the i-th data point, while $L - N$ are the degrees of freedom (i.e., number of data points minus number of parameters).

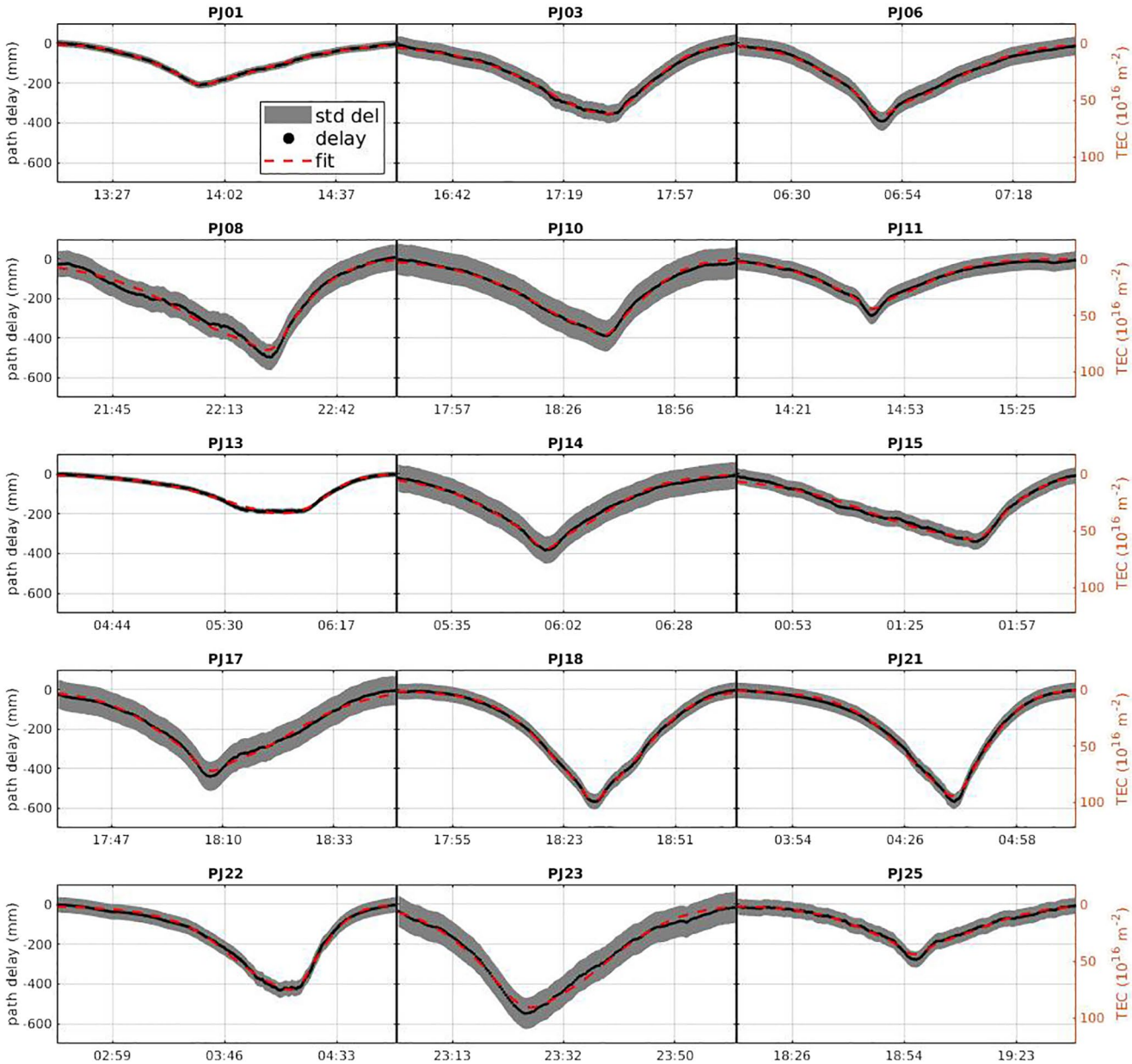

Figure 5. Path delay (black line) and associated uncertainty (gray area) with the fit of Equation 13 performed using the single arc approach (red dashed line). The path delay of PJ 01 and 13 was acquired with an incomplete link, hence it takes into account only the downlink plasma contribution.

The global solutions undergo a stability test in order to verify the uncertainties (whose details can be found in the Supporting Information S1). We made use of such test to correctly evaluate the uncertainty of our results.

3.1. Single Arc Fits

In this section, we present the fit we obtained with the single arc approach described in Section 2.4. The single arc approach is not able to decouple the radial position of the two region of the IPT (R_1 and R_2) from their respective offsets (Z_1 and Z_2) and the peak densities (N_1 and N_2) from the radial width (W_1 and W_2) in Equation 15, therefore we fixed $R_1 = 5.2R_J$, $R_2 = 5.7R_J$, $W_1 = 0.2R_J$ and $W_2 = 1.5R_J$. Thus there are six free parameters for each PJ, that are the peak density of the cold and outer torus N_1 and N_2, the vertical scale

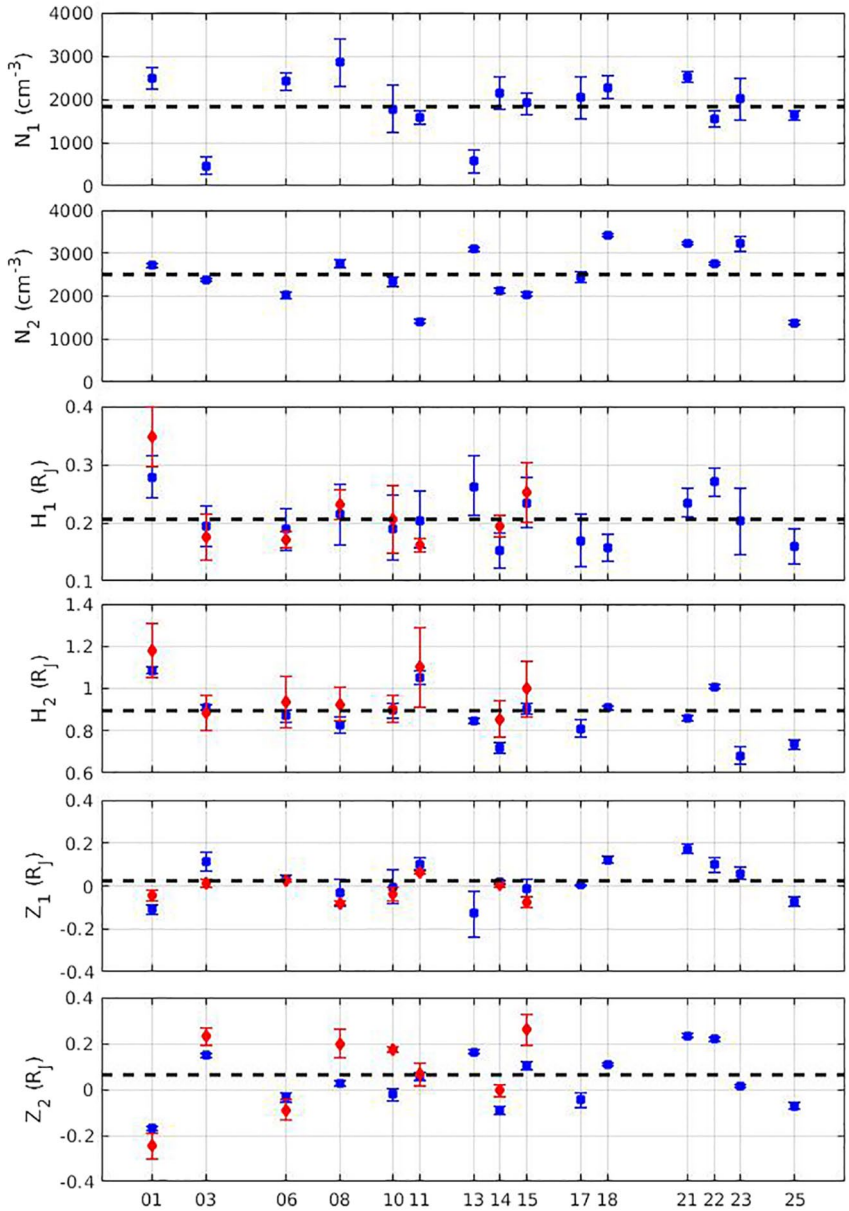

Figure 6. Plot of the parameters obtained with the single arc approach using Equation 13 with $R_1 = 5.2R_J$ and $R_2 = 5.7R_J$. The blue squares represents results from this work, which is based on JRM09, while the red diamonds are comparison for H_1, H_2, Z_1 and Z_2 from Phipps et al. (2021), whose reference magnetic field model is VIP4. The black dashed line is the weighted average. The corresponding PJ is reported on the abscissa.

height H_1 and H_2 and the offsets Z_1 and Z_2. The fit to each occultation can be seen in Figure 5: as can be noticed, the fits agree almost completely with the data within the uncertainty.

The parameters we obtained for each PJ are graphically displayed in the plots in Figure 6 alongside with their weighted average. A table with the same results can be inspected in the Supporting Information S1. Comparing the two top panels for N_1 and N_2, the cold torus exhibits density fluctuations mostly between 1,500 and 3,000 cm^{-3}, with an average of about 1800 cm^{-3}. Two noticeable exceptions are observed during PJ 03 and PJ 13, when the density of the cold torus fell below 500 cm^{-3}. On the other side, the density of the outer torus lies between 2,000 and 3,200 cm^{-3}, but during PJ 11 and 25 it dropped to ~1,300 cm^{-3}. The resulting average is about 2,500 cm^{-3}.

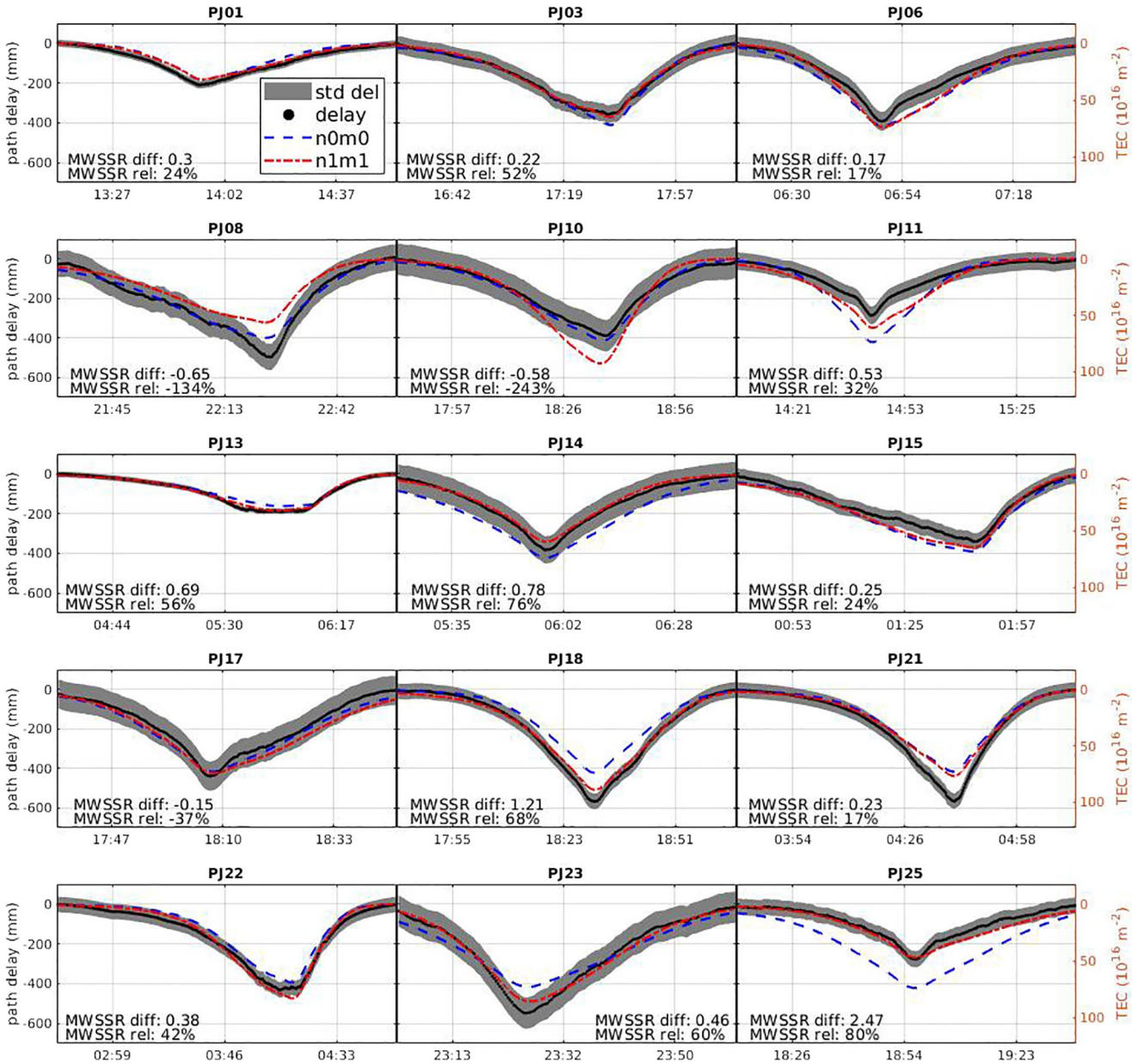

Figure 7. Black line: the same path delay as in Figure 5. Blue dashed line: fit of the path delay using the axisymmetric model (n0m0) for the density and the scale height. Red dot-dashed line: comparison with the mixed model (n1m1). In each panel is also reported the improvement of the weighted residuals MWSSR.

The scale height of the two regions exhibits also variations. H_1 ranges mainly between 0.15 and 0.3R$_J$. H_2 revealed that the thickness of outer torus varies noticeably during the Juno mission. The scale height remains mostly between 0.7 and 0.9R$_J$, but PJ 01, 11, and 22 are exceptions, with H_2 ranging between 1 and 1.1R$_J$. On average, the two average scale height are 0.21R$_J$ for the cold torus and 0.90R$_J$ for the outer one.

The offset of the cold torus span the range between -0.1R$_J$ and 0.2R$_J$, while Z_2 spread out in the range between -0.15R$_J$ and 0.25R$_J$. The average of the offset is about 0.03R$_J$ and 0.05R$_J$ for the cold and outer torus respectively.

If we compare the results we obtained for PJ01, 03, 06, 08 10, 11, 14, and 15 with the work of Phipps et al. (2019, 2021), the values of N_1 are compatible with previous analyses within 3 sigmas, while the values of N_2 agree within one sigma. The values of H_1 and H_2 we retrieved are compatible within one sigma with previous analyses (Phipps et al., 2019, 2021), except for H_2 during PJ 14, which is compatible within two

sigmas. Such differences may be due different method for the removal of the background. Indeed, the fiducial range of each occultation we choose may be different from other analyses. Besides, we substituted the signature of the IPT with a straight line before removing the background, which can also affect partially the resulting data. Our results for the offset differs from the of Phipps et al. (2019, 2021) because of the different frame: we adopted a centered dipole tilted by 6.8°, while they used an offset dipole tilted by 6.3°. Taking into account this difference (which accounts up to $\sim 0.07 R_J$ depending on the longitude), the results are compatible within one sigma for the cold torus, while for the outer torus the offsets are in agreement within three sigmas. The only exception is PJ 10, when the offset we obtained is different from the reference analysis (Phipps et al., 2021) by more the three sigmas.

3.2. Global Fits

The results reported in the remainder of this section are obtained using the global approach described in Section 2.4. Nevertheless, we retained the offsets Z_1 and Z_2 as local parameters, since the longitudinal and temporal variability that we will introduce in Section 3.2.2 involve only the density and the scale height. This choice helped to align the fitted path delay with the signature in the data, which is particularly relevant for the cold torus: indeed, its size (i.e., H_1) can be similar to its offset, therefore neglecting the variability of the offset shown in Figure 6 may strongly affect the determination of the density and scale height of the cold torus. Even though this effect should be less significant for the outer torus, it can still affect the shape of this region, especially for large offset as the ones observed during PJ 01, 21, and 22.

3.2.1. Axisymmetric Model

The axisymmetric model fits the data in Figure 5 using Equation 15, where all the parameters are constant over time and longitude. The results in this section were used as a reference and as input for the mixed models. As can be seen by the plots in Figure 7, such model cannot reproduce well all the observed data. In some occultations, the difference between the observed and fitted path delay is as large as 100 mm (e.g., PJ08, 11, 18, 21, 23, and 25). In addition, the width of the signature is very poorly represented by this model in multiple occasions (e.g., PJ14, 18, 21, 22, and 25). Nevertheless, the axisymmetric model can be viewed as an estimate of how the IPT looks like on average during the Juno mission.

As explained in Section 2.3, the global approach allowed us to retrieve the radial position of the IPT by exploiting the little tilt of the S/C-G/S line of sight with respect to the centrifugal plane. The value of $R_1 = 5.20 \pm 0.06 R_J$ matches the one found in literature (e.g., Bagenal et al., 1997; Dougherty et al., 2017) within the uncertainty. The value $R_2 = 5.73 \pm 0.05 R_J$ lies in the region where the peak density of the ribbon and the warm torus were observed by Voyager 1 (Bagenal & Sullivan, 1981) and Galileo (Bagenal et al., 1997).

The value of $N_1 = 1783 \pm 239 cm^{-3}$ and $N_2 = 2554 \pm 105\, cm^{-3}$ are very similar to the average we obtained from the single arc fits. Despite this, it is evident from Figure 7 that this value for N_2 does not represent suitably all our data set and discrepancies of more than 150 mm between fitted and observed delay can be noticed.

The values of $H_1 = 0.20 \pm 0.03 R_J$ and $H_2 = 0.90 \pm 0.03 R_J$ agree with previous models based on past missions (Bagenal, 1994; Bagenal et al., 1997) and with data analysis on the first PJs of Juno (Phipps et al., 2019, 2021). They are also compatible with the results from the single arc fits. Nevertheless, it is clear from Figure 7 that H_2 overestimates or underestimates the thickness of the torus during PJ 06, 11, 14, 18, 23, and 25.

The results of the axisymmetric model are reported in the last three columns of Table 2.

The offset Z_1 and Z_2 were considered as local parameters and they are not reported in Table 1, but they agree with the offsets retrieved from the single arc approach within one sigma.

3.2.2. Second Order Mixed Model

We finally present the result we obtained from the mixed model, whose Fourier coefficients are obtained from Equation 14 by taking $M_{max} = N_{max} = 1$. The expansion for N_2 reads

$$N_2 \rightarrow N_2\left[1 + A_{10}^{N_2}cos\lambda + B_{10}^{N_2}sin\lambda + A_{01}^{N_2}cos\left(\frac{2\pi t}{T}\right) + C_{01}^{N_2}sin\left(\frac{2\pi t}{T}\right) + \right.$$
$$+ A_{11}^{N_2}cos\lambda cos\left(\frac{2\pi t}{T}\right) + B_{11}^{N_2}sin\lambda cos\left(\frac{2\pi t}{T}\right) + \qquad (17)$$
$$\left. + C_{11}^{N_2}cos\lambda sin\left(\frac{2\pi t}{T}\right) + D_{11}^{N_2}sin\lambda sin\left(\frac{2\pi t}{T}\right)\right]$$

and the same holds for H_2. The total density and scale height need to be bounded in order to avoid potential negative values that might artificially result from the fit. In order to include this constraint we adopted a penalty function (Kuri-Morales & Gutiérrez-García, 2002) in our calculations. Therefore any set of parameters explored by the MCMC algorithm that does not satisfy the constraint is graded much less poorly than anyone that provides positive density and scale height. Additional details on this penalty function can be found in the Supporting Information S1.

This model takes into account both longitudinal and temporal variations of the IPT: this feature arises only from the second order and beyond because both M_{max} and N_{max} are different from zero. Equation 17 can be casted in the form

$$N_2\left[1 + \Delta N_\lambda cos(\lambda - \phi_{\lambda,N}) + \Delta N_T cos\left(\frac{2\pi t}{T} - \phi_{T,N}\right) + W_N(t)cos(\lambda - \phi_N(t))\right] \qquad (18)$$

where

$$\Delta N_\lambda = \sqrt{(A_{10}^{N_2})^2 + (B_{10}^{N_2})^2} \quad , \quad \phi_{\lambda,N} = atan\left(\frac{B_{10}^{N_2}}{A_{10}^{N_2}}\right)$$
$$\Delta N_T = \sqrt{(A_{01}^{N_2})^2 + (C_{01}^{N_2})^2} \quad , \quad \phi_{T,N} = atan\left(\frac{C_{01}^{N_2}}{A_{01}^{N_2}}\right) \qquad (19)$$

$$W_N^2(t) = \left[A_{11}^{N_2}cos\left(\frac{2\pi t}{T}\right) + C_{11}^{N_2}sin\left(\frac{2\pi t}{T}\right)\right]^2 + \left[B_{11}^{N_2}cos\left(\frac{2\pi t}{T}\right) + D_{11}^{N_2}sin\left(\frac{2\pi t}{T}\right)\right]^2 \qquad (20)$$

and

$$\phi_N(t) = atan\left[\frac{B_{11}^{N_2}cos\left(\frac{2\pi t}{T}\right) + D_{11}^{N_2}sin\left(\frac{2\pi t}{T}\right)}{A_{11}^{N_2}cos\left(\frac{2\pi t}{T}\right) + C_{11}^{N_2}sin\left(\frac{2\pi t}{T}\right)}\right] \qquad (21)$$

The mixed model then consists of a longitudinal modulation at fixed longitude (second term in Equation 18), a temporal pulsation (third term) and a longitudinal modulation whose amplitude and phase vary over time (fourth term).

The introduction of both longitudinal and temporal variations in our model led to a remarkable improvement of the fit, as can be noticed by looking at Figure 7. All the PJs except PJ08, 10, and 17 are better fitted using this model compared to the other global fits. This is particularly evident for PJ11, 13, 14, 22, 23, and 25. The overall MWSSR improved by 40% compared with the reference model.

The value of the zero order parameters in Table 2 are slightly different from what we obtained with the axisymmetric model. The peak density of the cold torus increased to $N_1 = 1993 \pm 185 cm^{-3}$, while N_2 decreased to $2429 \pm 68 cm^{-3}$ compared to the axisymmetric model. Despite these differences, the densities of the two models remains compatible within one sigma.

Also, the radial positions R_1 and R_2 as well as the scale height H_1 and H_2 are compatible with the reference model within the uncertainties. The offsets (not shown) are also in agreement with the results from the single arc fits.

In Table 3, we reported the amplitudes and phases of the first order corrections in the mixed model. We found that density and scale height are nearly anticorrelated. Looking at the phases of the longitudinal correction $\phi_{\lambda,N} = 133 \pm 4°$ and $\phi_{\lambda,H} = 20 \pm 17°$, we see they are separated by about $113 \pm 21°$, while for the

temporal correction we have $\phi_{T,N} = 310 \pm 20°$ and $\phi_{T,H} = 135 \pm 25°$, which are separated by $175 \pm 45°$. The corrections of the first order are quite important, as density fluctuations can be as high as 0.5 times the average, while the scale height can vary by about 0.3 times the average (taking into account both temporal and longitudinal variability). The amplitude we obtained at the first order showed that longitudinal modulation are more important than temporal one at the first order for the density, but they are both relevant for the scale height. Indeed, we obtained that $\Delta N_\lambda \approx 3\Delta N_T$, while $\Delta H_\lambda \approx \Delta H_T$. This is not in contrast with the fact that we observed PJs with large difference in the minimum path delay at nearly the same longitude. First, we still need to discuss the role of the second order correction. Second, those observations cannot be explained by a purely longitudinal modulation and require a temporal variability of the IPT. At the same time, temporal variability does not rule out longitudinal variation, which can then be retrieved if the model also includes pulsations and/or other time dependant changes in the IPT.

In Figure 8, we plotted the second order amplitude ($W_N(t)$ and $W_H(t)$ from Equation 20) and phase difference for density and scale height ($\phi_N(t) - \phi_H(t)$ from Equation 21). Looking at the plot of the evolution of amplitude over time for the second order correction of density and scale height (top panel in Figure 8), we can notice that the peak of the density fluctuation occurs about 50 days later than the peak in scale height. Comparing the maxima of both these curve with the corresponding first order amplitude in Table 3, it is evident that the second order contributions can be as relevant as the first order ones. The phase difference between density and scale height at the second order (bottom panel in Figure 8) lies almost always between 90° and 270°, as can be seen in the bottom panel in Figure 8. The phase Equation 21 in the bottom plot of Figure 8 slowly drifts periodically from ∼100° to ∼260°, which points out that the density and the scale height are almost anticorrelated.

In the top panels of Figure 9, we showed the color-coded density and scale height computed using Equation 18 with the retrieved parameters (the vertical axis spans a single period of 432 days). As can be seen, the mixed model revealed high temporal and longitudinal fluctuations. In the middle panels of Figure 9 we showed the density and scale height relative fluctuation as functions of time at specific longitudes $\lambda = 240°$ and $\lambda = 10°$, while in the bottom panels there are the fluctuations as functions of longitude at $t = 350$ and $t = 150$ days. As can be noticed, the two quantities are usually anticorrelated ($\lambda = 10°$ and $t = 150$ days), but sometimes they are nearly correlated ($\lambda = 240°$ and $t = 350$ days). The anticorrelation seems to occur mostly when the amplitude of the scale height fluctuations is higher.

The period we obtained with the mixed model is $T = 432 \pm 2$ days. This is about 5% less than the periodicity of the volcanic activity of Loki Patera retrieved by de Kleer et al. (2019) and about 6% and 10% less than the evolution timescales for the semimajor axis and eccentricity of Io's orbit, but nevertheless it can be considered as in indication that the IPT undergoes temporal variation on a similar timescale.

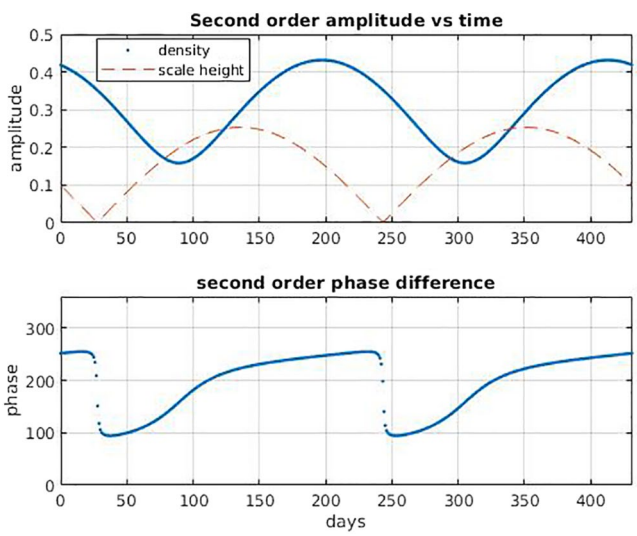

Figure 8. Top panel: plot of the second order amplitude of density (blue) and scale height (red dashed) as they change over time. Bottom panel: phase difference between $\phi_N(t)$ and $\phi_H(t)$.

4. Discussion

From the single arc fits we found that each set of parameter greatly varies from one occultation to the other, which point out that the IPT undergoes substantial changes over few weeks. Indeed, the density of the cold torus varies considerably from PJ03 ($N_1 \approx 500 cm^{-3}$) to PJ08 ($N_1 \approx 2900 cm^{-3}$). The mean density of the cold torus from the single arc approach was 1,800cm^{-3} (weighted with the uncertainty), ranging mostly between 1,500cm^{-3} and 25,00cm^{-3}. This value is in good agreement with the electron density at about 5.2R$_J$ from re-analysis of Voyager 1 data (Bagenal, Dougherty, et al., 2017) and about 800 cm^{-3} higher than the density measured by Galileo (Bagenal et al., 1997). The cold torus exhibit strong enhancements, like during PJ 01, 08, and 21, and depletions, like PJ 03 and 13. The outer torus shows an average density of 2,500cm^{-3} ranging mostly between 2,000cm^{-3} and 3,200cm^{-3}, except during PJ11 and PJ25, when the outer torus appeared much less dense (about 1300cm^{-3}). Such difference during those occultations is evident also by looking at the path

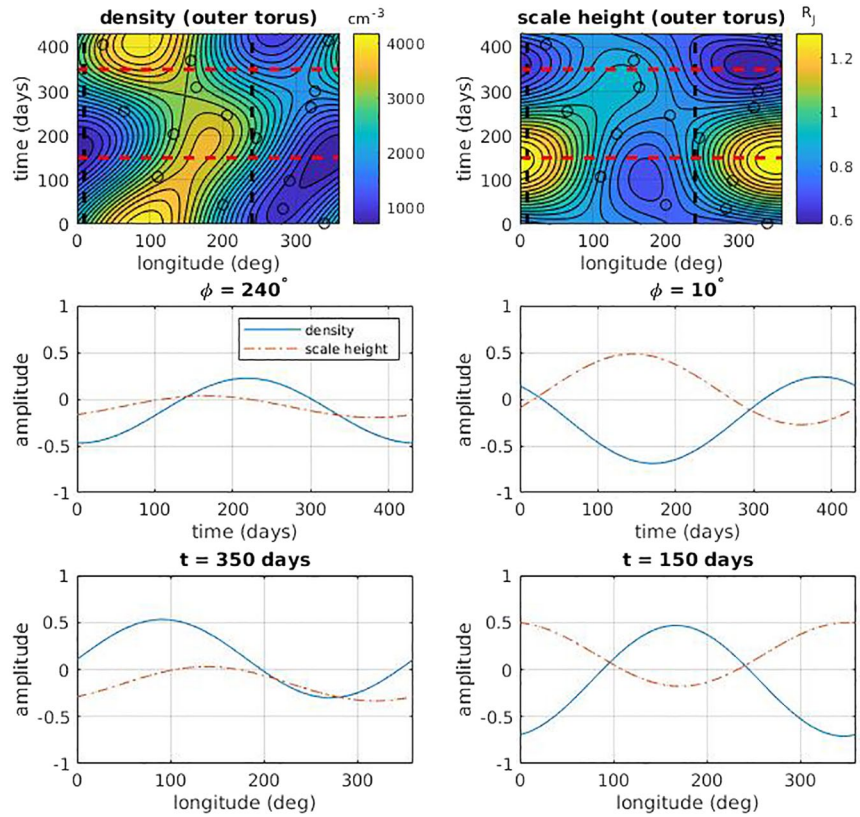

Figure 9. Top left panel: density predicted by the mixed model as a function of both time and longitude (Equation 18). The black dashed vertical lines are the cuts reported in the middle panels, the red dashed horizontal lines are reported in the bottom panels. The black circles represent each PJ. Top right panel: scale height predicted by Equation 18. Middle and bottom left panel: density and scale height correlation at 240° and $t = 350$ days from PJ01. Middle and bottom right panel: density and scale height anticorrelation at 10° and $t = 150$ days.

delay in Figure 5. The average density of the outer region from the global approach is also consistent with data from Voyager 1 (Bagenal & Sullivan, 1981), but about 600cm^{-3} lower than the data from Galileo (Bagenal et al., 1997). This may point out that the density of outer region of the IPT is more stable around 2,500 cm^{-3}, but occasional enhancement or depletion can occur.

Some of the PJs occurred at similar longitudes (see Figure 4), therefore we were able to observe that PJ03 and 13 exhibited very depleted cold torus during both occultations, which occurred at about 70°. On the other side, there are evidence of density variation in the cold torus, as can be seeing by comparing PJ11 and 18, which occurred at about 250°. The outer torus also showed different peak density values at similar longitudes, as can be noticed by comparing PJ11-18 and PJ06-23. This suggest that density variations of the IPT are time-dependant, although this does not rule out the possibility of longitudinal modulations. This is in agreement with the different electron density measured by Voyager 1 with respect to Galileo (Thomas et al., 2004).

In our models, we did not take into account the presence of the ribbon between the cold and the outer torus. This region has limited radial extent (<0.1R$_J$) and high density (3,000–4,000cm^{-3}), although this region showed longitudinal and temporal variability in both density and temperature (Thomas et al., 2004). Besides, this feature does not seems to be always present (Bagenal et al., 1997). The vertical extent of the ribbon is comparable with the outer torus (Bagenal, 1994; Phipps et al., 2018;

Table 3
Summary of the Amplitude and Phase of the First Order Corrections of the Mixed Model

params	*fit. val.*	*1 – sigma*
ΔN_λ	0.42	0.04
ΔH_λ	0.11	0.03
ΔN_T	0.13	0.03
ΔH_T	0.18	0.04
$\phi_{\lambda,N}$	133°	4°
$\phi_{\lambda,H}$	20°	17°
$\phi_{T,N}$	310°	20°
$\phi_{T,H}$	135°	25°

Phipps & Withers, 2017), thus its signature is mixed with the signature of the outer regions. In order to approximately estimate the relative contribution of the three regions of the outer torus in Equation 12, we can integrate this equation along lines parallel to the centrifugal equator, which is equivalent to Equation 17 in Phipps and Withers (2017). Taking the values of Voyager 1 from Table 2 of Phipps and Withers (2017) as a reference, the relative contributions to the TEC of the outer torus are approximately 10%, 32%, and 58% for the ribbon, warm torus and extended torus respectively. Although a single gaussian is not well suited to fit the radial profile of the electron density compared to a three-gaussian model, as showed in Figure S3, the best fit values in both cases would lead to a similar TEC for the occulting geometry of Juno. Therefore, the above-mentioned proportions we estimated from Voyager can be used to approximately retrieve the density of the ribbon, the warm and the extended torii as follow: first, we estimate the TEC using $N_2 \sim 2500 cm^{-3}$ and $R_2 \sim 5.7 R_J$ from Table 2 and $W_2 = 1.5 R_J$ as

$$TEC(z=0) \approx \frac{\sqrt{\pi}}{2}\left[N_2 W_2\left(1 - \frac{R_D - R_2}{W_2}\right)\right] \tag{22}$$

which is obtained from Equation 15 setting $m = 0$ and approximating the error function using $erf(x) = x$ for $|x| < 1$ and $erf(x) = 1$ for $x > 1$. R_D is the discontinuity at 5.5R$_J$. Then, the TEC due to the ribbon, the warm and the extended torus are evaluated according to the respective estimated proportions. Finally, the peak density is retrieved for each region using the above equation where R_2 and W_2 must be replaced with the values in Table 2 of Phipps and Withers (2017), while R_D must be set at $6.1 R_J$ as in Equation ~12. The resulting density of the ribbon is 2600cm^{-3}, while for the warm and extended torus we found ~2500cm^{-3} and ~1900cm^{-3} respectively. Therefore, the peak density we found using a single gaussian model for the outer torus closely matches the peak density of the ribbon and the warm torus estimated using three gaussians to model the same region. Nevertheless, these estimates should be taken as a rough indication, as the relative contribution of the three outer regions could change over time.

The scale height also showed substantial variability in both region we modeled. From the single arc fits, H_1 ranges nearly between 0.15R$_J$ and 0.3R$_J$, with an average of 0.2R$_J$. The average thickness of the outer torus was found to be H_2 about 0.9R$_J$, but we observed fluctuations up to nearly 1.1R$_J$ and down to less than 0.7 R$_J$. Being a proxy of the parallel electron temperature (Thomas, 1992), the changes in scale height in the two regions points out changes in the torus temperature. The relation between parallel temperature and scale height can be roughly estimated by $H \sim \sqrt{T_{\|}}$, thus a change in the thickness of the IPT from $H_2 = 0.7 R_J$ (e.g., PJ14) to $H_2 = 1.0 R_J$ (e.g., PJ22) implies that the temperature is nearly doubled. Besides, the scale height of the outer torus varies by 0.1–0.2R$_J$ between PJs which spanned similar sectors in Figure 4, like PJ01-17, PJ06-23, PJ10-22, and PJ11-18.

The offsets we retrieved showed that the IPT almost always lies above or below the nominal centrifugal equator by up to 0.25R$_J$. Indeed, the magnetic field due to quadrupole and higher moments as well as the inclusion of a plasma sheet model can systematically affect the vertical displacement of the IPT. In particular, the radial position of the torus affects the offset because of the warping of the centrifugal plane (Phipps et al., 2020). Besides, different offsets were retrieved at similar longitudes, such as during PJ 01 and 17 or PJ 10 and 22: this may be due to dusk-dawn asymmetries in the radial distance, which in turn can affect the offset in a centrifugal frame (Herbert et al., 2008; Schneider & Trauger, 1995).

Using the global approach we fit all the occultations with a single set of common parameters, except for the offsets Z$_1$ and Z$_2$, which were retained as local parameters. The parameters we found using the axisymmetric model in Section 3 can be regarded as describing the "average" torus during the Juno mission. We found that the density of $1783 \pm 239 cm^{-3}$ for the cold torus is similar to the average density obtained from the single arc fits. Besides, this value is quite in agreement with the one observed at the same distance by Voyager 1 but higher by about 700cm^{-3} than the data from Galileo (Bagenal et al., 1997). This difference may be due to the fact that those spacecrafts did not crossed the peak density in the cold torus. Indeed, because the cross section of this region is only 0.2–0.3R$_J$, it is possible that Voyager 1 and Galileo missed the peak density and passed about 0.1–0.2R$_J$ below or above the peak. This is enough to measure a density drop of about 20%–50% from the peak value. The density of the outer torus is also comparable between the single arc and the global fits. The value of N_2 is only 10% higher than the Voyager 1 measurement and about 50% lower than the density from Galileo at 6R$_J$. Taking into account that the scale height of the outer region is

about 0.9–1R$_J$, the measurements from those past missions represent closely the peak density of the IPT, thus we believe that differences with our result are indicative of variability in the density of the outer torus.

The results we obtained for the scale height H_1 and H_2 from the axisymmetric model are in good agreement with the average from the single arc fits. Indeed, the values of these parameters in Figure 6 lies mostly in the ranges 0.15–0.3R$_J$ and 0.7–1.1R$_J$ respectively. Both results are similar to the values found from previous analysis of the first PJs (Phipps et al., 2019). Nevertheless, the results from the global fit in Figure 7 showed poor agreement with the data. In particular, during PJ 14, 23, and 25 the scale height, which governs the width of the signature, overestimates the length of the occultation, while during PJ18, 21, and 22 it is underestimated.

Using the global fit we were able to include the radial positions R_1 and R_2 as free parameters. The value we obtained $R_1 = 5.20 \pm 0.06 R_J$ is in good agreement with the observations from Voyager 1 and Galileo, while $R_2 = 5.73 \pm 0.05 R_J$ lies in the region between 5.5 and 6 R$_J$ where the peak density of the ribbon and the warm torus are expected to occur. In our model, we did not take into account the offset of the magnetic equator with respect to the center of mass, which is given by $R_{offset} = 0.1 R_J$ at approximately 10° latitude and about 150–200° System III longitude (Connerney, 1993; Dessler, 1983). Including this offset, the torus is displaced by about $\pm 0.1 R_J$ along the offset vector. Nevertheless, the inclusion of such offset doesn't change substantially our results.

The offsets retrieved from the global fit with the axisymmetric model agree with the results from the single arc fit within the uncertainty.

The mixed model, which includes both temporal and longitudinal variability, showed the residuals were improved by about 40%. The predicted amplitude of the density fluctuations is large enough to explain the observed variability of the path delay, whose minima range between −300 and −600 mm. Indeed, we can see that all the values for N_2 and H_2 obtained with the single arc approach in Figure 6 fall within the extrema predicted by the mixed model in the top panels of Figure 9. The density of the cold torus we retrieved from both the axisymmetric and the mixed model agrees with previous estimate based on Juno data (Phipps et al., 2018, 2019, 2021), but they appears higher than the results from Galileo (Bagenal et al., 1997). The average density of the outer torus is also very similar to past in-situ observation of the IPT (Bagenal et al., 1997; Bagenal & Sullivan, 1981), but we retrieved wide fluctuations that can reach up to 70% of the average. Cassini recorded longitudinal variations in the electron density of about 20% (Steffl et al., 2006), while volcanic active periods can lead to a density increase by about 20%–25% (see for example Yoshioka et al., 2018). Our measurements are sensitive to the TEC, therefore it is possible that the fluctuations we retrieved are partially due to variation of the radial extension of the IPT, as the path delay depends on the TEC.

As a rough approximation, we expect the density and scale height to be nearly anticorrelated because they are related to the temperature by $N \sim T^{-1}$ while $H \sim \sqrt{T}$. The mixed model is the only model we tested which reproduced this feature, at least when the amplitude of the corrections is quite large. Nevertheless, the anticorrelation should not be taken too strictly. The relation between density and temperature $NT = constant$ holds if a polytropic equation of state is a proper choice for the plasma in the IPT, which relies on the assumption that density and temperature variations take place at constant pressure. Besides, the scale height depends on the temperature anisotropy (i.e., the ratio between perpendicular and parallel temperature of the plasma), on the parallel temperature and on the ambipolar electric field (Thomas, 1992), which in turn depends on the ion composition. While we found no indications that the anisotropy varies substantially over time, comparison between Voyager 1, Cassini and Galileo seems to point out that the ion composition can change at different epochs (Nerney et al., 2017). If such changes occur almost simultaneously with temperature variations, the resulting scale height is caused by both phenomena and not just by temperature variation. In the end, nonstationary injection of gas from Io into the torus may lead to transient states during which the anticorrelation between density and scale height is not mandatory. The anticorrelation should hold more strictly when the supply of plasma is quite steady and the ion composition does not change appreciably.

The best fit period for the mixed model is $T = 432 \pm 2$ days. We re-run the fit with the mixed model changing the initial value of T to check the stability of this result. We chose $T = 400$, 500, and 550 days and

the result remains compatible with $T = 432 \pm 2$ days. This period is quite similar to the periodicity of the activity of Loki Patera, which is taken as proxy for the overall volcanic activity on Io (de Kleer et al., 2019; Tsuchiya et al., 2019). In Figure 10, the infrared emission of Loki Patera is plotted as function of time alongside the average density of the outer torus predicted by the mixed model. Far from establishing a definitive connection between the morphology of the IPT and the volcanism of Io, nonetheless the similarity between our result and the periodicity of Loki is quite remarkable. In addition, Hisaki reported increased volcanic activity during the periods March–April 2015 and May–June 2016 (Tsuchiya et al., 2019). These events were observed alongside the decrease of the rotation period of IPT and increase in thermal electron temperature. Furthermore, the increased activity observed in the early 2015 was concurrent with an increased hot electron fraction (Hikida et al., 2020), which can affect the ionization of the main elements in the IPT (Steffl et al., 2006) and potentially its electron content as a consequence. Yoshioka et al. (2018) retrieved the radial profile of the electron and ion densities that matched the spectrum observed by the EXCEED instrument, onboard Hisaki, in the same period, showing that the electron peak density at ~6R_J can increase up to ~20%. The above-mentioned period observed by Hisaki occurred after the peak emissions from Loki Patera, as can be seen in Figure 10. Hikida et al. (2020) and Tsuchiya et al. (2019) suggested that Kurdalagon Patera and Pillian Patera may also be involved in the enhanced volcanic activity detected in 2015. Comparing the epochs observed by Hisaki, the activity of Loki Patera and the present prediction, we noticed that the electron density of the IPT starts to increase after that the emission from Loki increased and that a second minor peak is reached after the periods of enhanced activity recorded by Hisaki. Our results seems to suggest a potential correlation of the electron content of the IPT with the periods of volcanic activity, observed from September 2013 to June 2018. Nevertheless, the dynamics response of the IPT to the time-variable volcanic activity of Io is not straightforward, hence conclusions should be drawn carefully, as we discussed in Section 2.2. Adding future occultations and including direct observations of volcanic activity might strengthen this indication in the future.

The improvement of the residuals, the anticorrelation between density and scale height and the potential agreement between our period and the volcanic activity place the mixed model as the best candidate among our models to describe the variability of the IPT during the Juno mission.

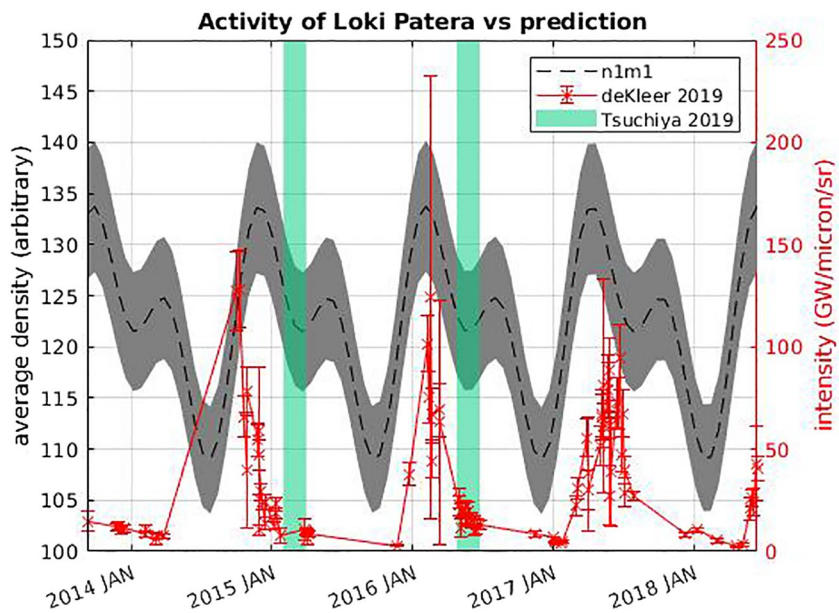

Figure 10. Infrared emission from Loki Patera (red crosses) taken from de Kleer et al. (2019) and average density of the outer torus predicted by the mixed model (black dashed line). The green shaded areas point out the periods of volcanic activity observed by Hisaki (Tsuchiya et al., 2019). The density is expressed in arbitrary units. The time axis spans from September 10th 2013 to June 25th 2018.

5. Conclusions

We made use of the path delay measured during 15 occultations of the Io plasma torus to inspect its morphology and variability, which was investigated by a Fourier expansion of a parametric model of the density distribution (Phipps & Withers, 2017). We assumed the IPT to be made by two regions: a cold inner torus and an outer warm torus, both of which were modeled by gaussian profiles in the radial and vertical direction (in cylindrical coordinates in a frame of reference tilted by 6.8° toward $\lambda_{III} \approx 200°$).

We integrated the density profile of the IPT along the line of sight between Juno and the DSN station and we obtain an analytical formula for the TEC, which is proportional to the path delay. The integration was carried out in an approximated 2-dimensional geometry, which introduced a small error (compared to the uncertainty) with respect to a full 3D integration. The result can be efficiently employed on iterative algorithms, such the Markov Chain Monte Carlo algorithm we used in this work (Haario et al., 2001, 2006). The equation we obtained takes into account the tilt of the line of sight with respect to the centrifugal equator, thus it can be used to retrieve the radial position and extent of the IPT, at least in principle. Actually, the radial extension and the peak density are strongly coupled by the geometry of the occultations, thus we needed to fix the radial extension (W_1 and W_2 in Equations 13 and 15).

We analyzed our data using two approaches: the single arc fit and the global fit. From the former we obtained peak density, vertical extension and offset from the centrifugal equator for each occultation. We needed to fix the radial position when using the single arc approach because the radial position and the vertical offset were strongly coupled by the geometry (this coupling is removed in the global fit). This method is the same as used in previous analysis of the IPT morphology during the Juno mission (Phipps et al., 2018, 2019, 2021). The densities we obtained are in agreement with previous analyses within three sigma for the cold torus and within 1 sigma for the outer torus. Deviations of the average values between previous and this studies may be due to the different fit to the background signal. Indeed, we enforce the background removal to follow a straight line in place of the signature of the IPT, which is different from what used by Phipps et al. (2019, 2021). This in turn may affect the depth of the signature. We also noticed that the offset deviates by about $\pm 1°$ with respect to the position predicted by a nominal centrifugal equator based on a dipolar magnetic field. As highlighted by Phipps et al. (2020), this suggest that the inclusion of higher-than-dipole moments of the magnetic field and the plasma disk should be taken into account to compute the centrifugal equator. Besides, the latitudinal distribution of plasma between 5 and 10 R_J is a function of the radial distance (Phipps et al., 2020), which should also be considered when evaluating the offset of the IPT.

The residuals obtained from te mixed model are about 40% better than the reference model. Besides, the density and scale height predicted by this model are mostly anticorrelated, even though correlation is still possible when the density and scale height show little fluctuations. This feature is appreciated, as we expect the density to be inversely proportional to the temperature, while the scale height to be proportional to the square root of the temperature. Lastly, the characteristic period we found of about 430 days is somewhat close to the periodicity in volcanic activity and orbital changes of Io recently investigated (de Kleer et al., 2019). Even though we do want to point out any hard evidence between volcanism on Io and the response of the IPT to the mass supply (which requires ad hoc theoretical modeling of the Io-IPT interaction and monitoring of the activity on Io, both of which are beyond the scope of our work), at least we take this as an indication of such potential interaction.

Without delving deeply into the physical interpretation of the results we obtained, we showed that both longitudinal and temporal variations of plasma in the IPT are likely to occur, which should be kept in mind in planning and analysing long-term missions in the Jupiter's inner magnetosphere.

Data Availability Statement

Spacecraft and DSN station data can be retrieved at https://naif.jpl.nasa.gov/naif/data.html. The Doppler data and ancillary information used in this analysis are archived in NASA's Planetary Data System (Buccino, 2016).

Acknowledgments
The authors are grateful to the Italian Space Agency (ASI) for financial support through Agreement No. 2018-25-HH.0 in the context of ESA's JUICE mission, and Agreement No. 2017-40-H.1-2020, and its extension 2017-40-H.02020-13-HH.0, for ESA's BepiColombo and NASA's Juno radio science experiments. The authors are grateful to Dustin Buccino and Ryan S. Park for their suggestions and careful proofreading of the manuscript.
Open Access Funding provided by Universita di Bologna within the CRUI-CARE Agreement.

References

Asmar, S. W., Bolton, S. J., Buccino, D. R., Cornish, T. P., Folkner, W. M., Formaro, R., et al. (2017). The Juno gravity science instrument. *Space Science Reviews*, *213*(1–4), 205–218. https://doi.org/10.1007/s11214-017-0428-7

Bagenal, F. (1994). Empirical model of the Io plasma torus: Voyager measurements. *Journal of Geophysical Research*, *99*(A6), 11043. https://doi.org/10.1029/93JA02908

Bagenal, F., Adriani, A., Allegrini, F., Bolton, S. J., Bonfond, B., Bunce, E. J., et al. (2017). Magnetospheric science objectives of the Juno mission. *Space Science Reviews*, *213*(1–4), 219–287. https://doi.org/10.1007/s11214-014-0036-8

Bagenal, F., Crary, F. J., Stewart, A. I. F., Schneider, N. M., Gurnett, D. A., Kurth, W. S., et al. (1997). Galileo measurements of plasma density in the Io torus. *Geophysical Research Letters*, *24*(17), 2119–2122. https://doi.org/10.1029/97GL01254

Bagenal, F., Dougherty, L. P., Bodisch, K. M., Richardson, J. D., & Belcher, J. M. (2017). Survey of Voyager plasma science ions at Jupiter: 1. Analysis method. *Journal of Geophysical Research: Space Physics*, *122*(8), 8241–8256. https://doi.org/10.1002/2016JA023797

Bagenal, F., & Sullivan, J. D. (1981). Direct plasma measurements in the Io torus and inner magnetosphere of Jupiter. *Journal of Geophysical Research*, *86*(A10), 8447–8466. https://doi.org/10.1029/JA086iA10p08447

Bertotti, B., Comoretto, G., & Iess, L. (1993). Doppler tracking of spacecraft with multi-frequency links. *Astronomy and Astrophysics*, *269*(1–2), 608–616.

Bigg, E. K. (1964). Influence of the satellite Io on Jupiter's decametric emission. *Nature*, *203*(4949), 1008–1010. https://doi.org/10.1038/2031008a0

Bird, M., Asmar, S., Edenhofer, P., Funke, O., Pätzold, M., & Volland, H. (1993). The structure of Jupiter's Io plasma torus inferred from Ulysses radio occultation observations. *Planetary and Space Science*, *41*(11–12), 999–1010. https://doi.org/10.1016/0032-0633(93)90104-A

Bird, M. K., Asmar, S. W., Brenkle, J. P., Edenhofer, P., Funke, O., Patzold, M., & Volland, H. (1992). Ulysses radio occultation observations of the lo plasma torus during the Jupiter encounter. *Science*, *257*(5076), 1531–1535. https://doi.org/10.1126/science.257.5076.1531

Bridge, H. S., Belcher, J. W., Lazarus, A. J., Sullivan, J. D., Bagenal, F., Mcnutt, R. L., et al. (1979). Plasma observations near Jupiter: Initial results from Voyager 2. *Science*, *206*(4421), 972–976. https://doi.org/10.1126/science.206.4421.972

Broadfoot, A. L., Belton, M. J. S., Takacs, P. Z., Sandel, B. R., Shemansky, D. E., Holberg, J. B., et al. (1979). Extreme ultraviolet observations from Voyager 1 Encounter with Jupiter. *Science*, *204*(4396), 979–982. https://doi.org/10.1126/science.204.4396.979

Brown, M. E. (1995). Periodicities in the Io plasma torus. *Journal of Geophysical Research*, *100*(A11), 21683–21695. https://doi.org/10.1029/95JA01988

Brown, R. A. (1976). A model of Jupiter's sulfur nebula. *Acta Pathologica Japonica*, *206*, L179. https://doi.org/10.1086/182162

Brown, R. A., & Chaffee, F. H., Jr (1974). High-resolution spectra of sodium emission from IO. *Acta Pathologica Japonica*, *187*, L125. https://doi.org/10.1086/181413

Buccino, D. R. (2016). *Juno Jupiter gravity science raw data set V1.0, JUNO-J-RSS-1-JUGR-V1.0*. NASA Planetary Data System.

Buccino, D. R., Border, J., Volk, C., & Yang, O. (2019). Measurement of station delay at DSS-25. *IPN Progress Report*, *42*, 217.

Connerney, J. E. P. (1993). Magnetic fields of the outer planets. *Journal of Geophysical Research*, *98*(E10), 18659. https://doi.org/10.1029/93JE00980

Cowles, M. K., & Carlin, B. P. (1996). Markov chain Monte Carlo convergence diagnostics: A comparative review. *Journal of the American Statistical Association*, *91*(434), 883–904. https://doi.org/10.1080/01621459.1996.10476956

Davies, A. G. (2001). Volcanism on Io: The view from Galileo. *Astronomy and Geophysics*, *42*(2), 2–10. https://doi.org/10.1046/j.1468-4004.2001.42210.x

de Kleer, K., Nimmo, F., & Kite, E. (2019). Variability in Io's volcanism on timescales of periodic orbital changes. *Geophysical Research Letters*, *46*(12), 6327–6332. https://doi.org/10.1029/2019GL082691

Delamere, P. A., Steffl, A., & Bagenal, F. (2004). Modeling temporal variability of plasma conditions in the Io torus during the Cassini era. *Journal of Geophysical Research*, *109*(A10). https://doi.org/10.1029/2003JA010354

Dessler, A. J. (Ed.), (1983). *Physics of the Jovian magnetosphere* (1st ed.). Cambridge University Press. https://doi.org/10.1017/CBO9780511564574

Dougherty, L. P., Bodisch, K. M., & Bagenal, F. (2017). Survey of Voyager plasma science ions at Jupiter: 2. Heavy ions. *Journal of Geophysical Research: Space Physics*, *122*(8), 8257–8276. https://doi.org/10.1002/2017JA024053

Durante, D., Parisi, M., Serra, D., Zannoni, M., Notaro, V., Racioppa, P., et al. (2020). Jupiter's gravity field halfway through the Juno mission. *Geophysical Research Letters*, *47*(4). https://doi.org/10.1029/2019GL086572

Ebert, R. W., Bagenal, F., McComas, D. J., & Fowler, C. M. (2014). A survey of solar wind conditions at 5 AU: A tool for interpreting solar wind-magnetosphere interactions at Jupiter. *Frontiers in Astronomy and Space Science*, *1*. https://doi.org/10.3389/fspas.2014.00004

Gurnett, D. A., Kurth, W. S., Roux, A., Bolton, S. J., & Kennel, C. F. (1996). Galileo plasma wave observations in the Io plasma torus and near Io. *Science*, *274*(5286), 391–392. https://doi.org/10.1126/science.274.5286.391

Haario, H., Laine, M., Mira, A., & Saksman, E. (2006). DRAM: Efficient adaptive MCMC. *Statistics and Computing*, *16*(4), 339–354. https://doi.org/10.1007/s11222-006-9438-0

Haario, H., Saksman, E., & Tamminen, J. (2001). An Adaptive metropolis algorithm. *Bernoulli*, *7*(2), 223. https://doi.org/10.2307/3318737

Herbert, F., Schneider, N. M., & Dessler, A. J. (2008). New description of Io's cold plasma torus. *Journal of Geophysical Research*, *113*(A1). https://doi.org/10.1029/2007JA012555

Hess, S. L. G., Delamere, P. A., Bagenal, F., Schneider, N., & Steffl, A. J. (2011). Longitudinal modulation of hot electrons in the Io plasma torus. *Journal of Geophysical Research*, *116*(A11). https://doi.org/10.1029/2011JA016918

Hikida, R., Yoshioka, K., Tsuchiya, F., Kagitani, M., Kimura, T., Bagenal, F., et al. (2020). Spatially asymmetric increase in hot electron fraction in the Io plasma torus during volcanically active period revealed by observations by Hisaki/EXCEED from november 2014 to May 2015. *Journal of Geophysical Research: Space Physics*, *125*(3), e2019JA027100. https://doi.org/10.1029/2019JA027100

Hill, T. W., Dessler, A. J., & Michel, F. C. (1974). Configuration of the Jovian magnetosphere. *Geophysical Research Letters*, *1*(1), 3–6. https://doi.org/10.1029/GL001i001p00003

Hinson, D. P., Kliore, A. J., Flasar, F. M., Twicken, J. D., Schinder, P. J., & Herrera, R. G. (1998). Galileo radio occultation measurements of Io's ionosphere and plasma wake. *Journal of Geophysical Research*, *103*(A12), 29343–29357. https://doi.org/10.1029/98JA02659

Iess, L., Di Benedetto, M., James, N., Mercolino, M., Simone, L., & Tortora, P. (2014). Astra: Interdisciplinary study on enhancement of the end-to-end accuracy for spacecraft tracking techniques. *Acta Astronautica*, *94*(2), 699–707. https://doi.org/10.1016/j.actaastro.2013.06.011

Koga, R., Tsuchiya, F., Kagitani, M., Sakanoi, T., Yoshioka, K., Yoshikawa, I., et al. (2019). Transient change of Io's neutral oxygen cloud and plasma torus observed by Hisaki. *Journal of Geophysical Research: Space Physics*, *124*(12), 10318–10331. https://doi.org/10.1029/2019JA026877

Köhnlein, W. (1996). Radial dependence of solar wind parameters in the ecliptic (1.1 R–61 AU). *Solar Physics*, *169*(1), 209–213. https://doi.org/10.1007/BF00153841

Kupo, I., Mekler, Y., & Eviatar, A. (1976). Detection of ionized sulfur in the Jovian magnetosphere. *Acta Pathologica Japonica*, *205*, L51. https://doi.org/10.1086/182088

Kuri-Morales, A. F., & Gutiérrez-García, J. (2002). Penalty function methods for constrained optimization with genetic algorithms: A statistical analysis. In Coello Coello, C. A., de Albornoz, A., Sucar, L. E., & Battistutti, O. C. (Eds.), *MICAI 2002: Advances in artificial intelligence* (pp. 108–117). Berlin, Heidelberg: Springer. https://doi.org/10.1007/3-540-46016-0_12

Lopes, R. M., & Williams, D. A. (2015). Volcanism on Io. In *The encyclopedia of volcanoes* (pp. 747–762). Elsevier. https://doi.org/10.1016/B978-0-12-385938-9.00043-2

Mariotti, G., & Tortora, P. (2013). Experimental validation of a dual uplink multifrequency dispersive noise calibration scheme for Deep Space tracking: Dual uplink incomplete link. *Radio Science*. *48*(2), 111–117. https://doi.org/10.1002/rds.20024

Matthaeus, W. H., Klein, L. W., Ghosh, S., & Brown, M. R. (1991). Nearly incompressible magnetohydrodynamics, pseudosound, and solar wind fluctuations. *Journal of Geophysical Research*, *96*(A4), 5421. https://doi.org/10.1029/90JA02609

McDoniel, W. J., Goldstein, D. B., Varghese, P. L., & Trafton, L. M. (2019). Simulation of Io's plumes and Jupiter's plasma torus. *Physics of Fluids*, *31*(7), 077103. https://doi.org/10.1063/1.5097961

Nerney, E. G., Bagenal, F., & Steffl, A. J. (2017). Io plasma torus ion composition: Voyager, Galileo, and Cassini. *Journal of Geophysical Research: Space Physics*, *122*(1), 727–744. https://doi.org/10.1002/2016JA023306

Phipps, P. H., & Withers, P. (2017). Radio occultations of the Io plasma torus by *Juno* are feasible. *Journal of Geophysical Research: Space Physics*, *122*(2), 1731–1750. https://doi.org/10.1002/2016JA023447

Phipps, P. H., Withers, P., Buccino, D. R., Yang, Y., & Parisi, M. (2019). Variations in the Density Distribution of the Io Plasma Torus as Seen by Radio Occultations on Juno Perijoves 3, 6, and 8. *Journal of Geophysical Research: Space Physics*, *124*(7), 5200–5221. https://doi.org/10.1029/2018JA026297

Phipps, P. H., Withers, P., Buccino, D. R., & Yang, Y.-M. (2018). Distribution of plasma in the Io plasma torus as seen by radio occultation during *Juno* Perijove 1. *Journal of Geophysical Research: Space Physics*, *123*(8), 6207–6222. https://doi.org/10.1029/2017JA025113

Phipps, P. H., Withers, P., Buccino, D. R., Yang, Y.-M., & Parisi, M. (2021). Two years of observations of the Io plasma torus by Juno radio occultations: Results from Perijoves 1 to 15. *Journal of Geophysical Research: Space Physics*, *126*(3), e2020JA028710. https://doi.org/10.1029/2020JA028710

Phipps, P. H., Withers, P., Vogt, M. F., Buccino, D. R., Yang, Y., Parisi, M., et al. (2020). Where Is the Io plasma torus? A comparison of observations by Juno radio occultations to predictions from Jovian magnetic field models. *Journal of Geophysical Research: Space Physics*, *125*(8). https://doi.org/10.1029/2019JA027633

Sandel, B. R., Shemansky, D. E., Broadfoot, A. L., Bertaux, J. L., Blamont, J. E., Belton, M. J. S., et al. (1979). Extreme ultraviolet observations from Voyager 2 Encounter with Jupiter. *Science*, *206*(4421), 962–966. https://doi.org/10.1126/science.206.4421.962

Scarf, F. L., Gurnett, D. A., & Kurth, W. S. (1979). Jupiter plasma wave observations: An initial Voyager 1 overview. *Science*, *204*(4396), 991–995. https://doi.org/10.1126/science.204.4396.991

Schneider, N. M., & Trauger, J. T. (1995). The structure of the Io Torus. *Acta Pathologica Japonica*, *450*, 450. https://doi.org/10.1086/176155

Smith, B. A., Soderblom, L. A., Johnson, T. V., Ingersoll, A. P., Collins, S. A., Shoemaker, E. M., et al. (1979). The Jupiter system through the eyes of Voyager 1. *Science*, *204*(4396), 951–972. https://doi.org/10.1126/science.204.4396.951

Steffl, A. (2004a). Cassini UVIS observations of the Io plasma torus. I. Initial results. *Icarus*, *172*(1), 78–90. https://doi.org/10.1016/j.icarus.2003.12.027

Steffl, A. (2004b). Cassini UVIS observations of the Io plasma torus. II. Radial variations. *Icarus*, *172*(1), 91–103. https://doi.org/10.1016/j.icarus.2004.04.016

Steffl, A., Delamere, P., & Bagenal, F. (2006). Cassini UVIS observations of the Io plasma torus III. Observations of temporal and azimuthal variability. *Icarus*, *180*(1), 124–140. https://doi.org/10.1016/j.icarus.2005.07.013

Steffl, A., Delamere, P., & Bagenal, F. (2008). Cassini UVIS observations of the Io plasma torus. *Icarus*, *194*(1), 153–165. https://doi.org/10.1016/j.icarus.2007.09.019

Thomas, N. (1992). Optical observations of Io's neutral clouds and plasma torus. *Surveys in Geophysics*, *13*(2), 91–164. https://doi.org/10.1007/BF01903525

Thomas, N. (1993). The variability of the Io plasma torus. *Journal of Geophysical Research*, *98*(E10), 18737. https://doi.org/10.1029/93JE01461

Thomas, N., Bagenal, F., Hill, T. W., & Wilson, J. K. (2004). The Io neutral clouds and plasma torus. In Bagenal, F., Dowling, T. E., McKinnon, W. B. (Eds), *Jupiter: The planet, satellites and magnetosphere* (pp. 561–591). Cambridge UK: Cambridge University PressW. B. McKinnon.

Thornton, C. L., & Border, J. S. (2000). Radiometric Tracking Techniques for Deep-Space Navigation (Vol. 1). Hoboken, N. J: Jet Propulsion Laboratory, California Institute of Technology.

Tsuchiya, F., Arakawa, R., Misawa, H., Kagitani, M., Koga, R., Suzuki, F., et al. (2019). Azimuthal variation in the Io plasma torus observed by the Hisaki satellite from 2013 to 2016. *Journal of Geophysical Research: Space Physics*, *124*(5), 3236–3254. https://doi.org/10.1029/2018JA026038

Tsuchiya, F., Yoshioka, K., Kimura, T., Koga, R., Murakami, G., Yamazaki, A., et al. (2018). Enhancement of the Jovian magnetospheric plasma circulation caused by the change in plasma supply from the satellite Io. *Journal of Geophysical Research: Space Physics*, *123*(8), 6514–6532. https://doi.org/10.1029/2018JA025316

Warwick, J. W., Pearce, J. B., Riddle, A. C., Alexander, J. K., Desch, M. D., Kaiser, M. L., et al. (1979). Voyager 1 planetary radio astronomy observations near Jupiter. *Science*, *204*(4396), 995–998. https://doi.org/10.1126/science.204.4396.995

Yoshikawa, I., Suzuki, F., Hikida, R., Yoshioka, K., Murakami, G., Tsuchiya, F., et al. (2017). Volcanic activity on Io and its influence on the dynamics of the Jovian magnetosphere observed by EXCEED/Hisaki in 2015. *Earth Planets and Space*, *69*(1), 110. https://doi.org/10.1186/s40623-017-0700-9

Yoshioka, K., Tsuchiya, F., Kagitani, M., Kimura, T., Murakami, G., Fukuyama, D., et al. (2018). The influence of Io's 2015 volcanic activity on Jupiter's magnetospheric dynamics. *Geophysical Research Letters*, *45*(19), 10193–10199. https://doi.org/10.1029/2018GL079264

Zannoni, M. (2020). Effects of ground station delays on plasma calibrations for Juno orbit determination. In *AIAA SCITECH 2020 forum*. Orlando, FL: American Institute of Aeronautics and Astronautics. https://doi.org/10.2514/6.2020-1699